J. Fluid Mech. (2003), *vol.* 474, *pp.* 1–33.
DOI: 10.1017/S0022112002002665 Printed in the United Kingdom

Coherent structures in oscillatory boundary layers

By PAOLA COSTAMAGNA, GIOVANNA VITTORI AND PAOLO BLONDEAUX

Environmental Engineering Department, University of Genova, Via Montallegro 1, 16145 Genova, Italy

(Received 28 February 2002)

The dynamics of the vortex structures appearing in an oscillatory boundary layer (Stokes boundary layer), when the flow departs from the laminar regime, is investigated by means of flow visualizations and a quantitative analysis of the velocity and vorticity fields. The data are obtained by means of direct numerical simulations of the Navier–Stokes and continuity equations. The wall is flat but characterized by small imperfections. The analysis is aimed at identifying points in common and differences between wall turbulence in unsteady flows and the well-investigated turbulence structure in the steady case. As in Jimenez & Moin (1991), the goal is to isolate the basic flow unit and to study its morphology and dynamics. Therefore, the computational domain is kept as small as possible.

The elementary process which maintains turbulence in oscillatory boundary layers is found to be similar to that of steady flows. Indeed, when turbulence is generated, a sequence of events similar to those observed in steady boundary layers is observed. However, these events do not occur randomly in time but with a repetition time scale which is about half the period of fluid oscillations. At the end of the accelerating phases of the cycle, low-speed streaks appear close to the wall. During the early part of the decelerating phases the strength of the low-speed streaks grows. Then the streaks twist, oscillate and eventually break, originating small-scale vortices. Far from the wall, the analysis of the vorticity field has revealed the existence of a sequence of streamwise vortices of alternating circulation pumping low-speed fluid far from the wall as suggested by Sendstad & Moin (1992) for steady flows. The vortex structures observed far from the wall disappear when too small a computational domain is used, even though turbulence is self-sustaining. The present results suggest that the streak instability mechanism is the dominant mechanism generating and maintaining turbulence; no evidence of the well-known parent vortex structures spawning offspring vortices is found. Although wall imperfections are necessary to trigger transition to turbulence, the characteristics of the coherent vortex structures, for example the spacing of the low-speed streaks, are found to be independent of wall imperfections.

1. Introduction

Quasi-coherent vortex structures are now considered to be ubiquitous features of wall turbulence and they have been much investigated during the past few years, providing a deep physical insight into the mechanisms controlling momentum, mass and heat transfer close to rigid boundaries in turbulent flows (see the contributions by Hussain 1986; Kline & Afgan 1988; Robinson 1991; Moin & Mahesh 1998).

However, attention has been mainly devoted to steady flows and many aspects of wall turbulence in unsteady flows are still unknown. The lack of a deep knowledge of unsteady turbulence is largely due to the difficulties encountered when making accurate measurements of turbulence characteristics in rapidly varying flows and in tackling the problem by analytical means. Moreover, few attempts to numerically simulate unsteady turbulent flows can be found into the literature, perhaps because of the difficulties in triggering transition to turbulence (Spalart & Baldwin 1988; Akhavan, Kamm & Shapiro 1991). However, unsteady flows are as important as steady ones and the investigation of turbulence structure in accelerating and/or decelerating flows may provide additional physical insight as well as raising additional questions regarding the origin and development of wall turbulence. Moreover the study of coherent vortex structures in unsteady flows, and in particular in oscillating or pulsatile flows, is of relevance in many engineering fields like biofluid dynamics, turbomachinery control, coastal engineering to cite a few.

In the present contribution we consider the unsteady boundary layer generated by an oscillating flow close to a fixed rigid wall (Stokes boundary layer), which can be considered as a prototype of unsteady boundary layers, and we investigate the vortex structures which appear during transition from the laminar to the turbulent regime and those characterizing wall turbulence at moderate values of the Reynolds number.

Previous studies of the Stokes boundary layer were concerned primarily with the identification of transition between the laminar and turbulent regimes and the investigation of the average characteristics of turbulence. As summarized and discussed in Vittori & Verzicco (1998) and Blondeaux & Vittori (1999), experimental results seem to indicate that transition does not take place at a well-defined Reynolds number, but it is a continuous process characterized by the appearance of small flow perturbations at a first critical value of the Reynolds number, which has not been precisely identified. When the Reynolds number is increased and becomes larger than a second critical value, these disturbances originate turbulence bursts, which however appear only during the decelerating phases of the cycle. Indeed, during the accelerating phases, the flow recovers a laminar-like behaviour. Further increases of the Reynolds number lead turbulence to appear earlier and to pervade larger parts of the cycle and eventually to be present throughout the whole cycle when the Reynolds number exceeds a third critical value. Hence, on the basis of the experimental results, four regimes can be identified: the laminar regime, the disturbed laminar regime, the intermittently turbulent regime and the fully turbulent regime.

The theoretical investigation of Blondeaux & Vittori (1994) and the numerical simulations of Spalart & Baldwin (1988), Verzicco & Vittori (1996) and Vittori & Verzicco (1998) along with the experimental results suggest that wall imperfections or other external sources of disturbances play a fundamental role in triggering the appearance of turbulence in oscillatory flows. By analysing the Stokes boundary layer over a wavy wall of small amplitude, Blondeaux & Vittori (1994) found that the flow deviates from the laminar regime because of the growth of perturbations, which takes place only at particular phases of the cycle due to a resonance mechanism which is present only when the Reynolds number is larger than a critical value equal to about 100 (herein the Reynolds number is defined as $R_\delta = U_0^* \sqrt{2\nu^*/\omega^*}/\nu^*$, where U_0^* and ω^* are the amplitude and the angular frequency of velocity oscillations far from the wall and ν^* is the kinematic viscosity of the fluid). This resonance mechanism leads to an energy transfer from the basic flow to the perturbations, which is induced by the wall waviness when the latter is characterized by a particular streamwise wavenumber that depends on the value of the Reynolds number (receptivity mechanism).

The analysis by Blondeaux & Vittori (1994) is two-dimensional and therefore it provides a possible explanation for the mechanism leading to the appearance of the first flow perturbations observed in the experimental investigations when R_δ exceeds 100; however, it cannot describe turbulence development and cannot explain the differences between the disturbed laminar regime and the intermittently turbulent one experimentally observed when the Reynolds number is larger than a critical value between 500 and 600.

Two possible explanations of the inception of the intermittently turbulent regime can be given. The first one is based on the numerical results by Akhavan *et al.* (1991), who found that for values of R_δ larger than about 500, three-dimensional perturbations can grow if a large two-dimensional wave pre-exists in the Stokes flow. This large-amplitude wave might be generated, for example, by the resonance mechanism described by Blondeaux & Vittori (1994). A second possible explanation is provided by Wu (1992) who showed that the amplitudes of two- and three-dimensional components of a small perturbation can develop a finite-time singularity. This explosive growth of the perturbation is possible when the Reynolds number is sufficiently large. Moreover the disturbance should be composed of a pair of oblique waves of small amplitude ϵ and wavenumbers equal to α and $\pm\sqrt{3\alpha}$ in the streamwise and spanwise directions respectively plus a two-dimensional wave with wavenumber 2α and an amplitude of order $\epsilon^{4/3}$. The direct numerical simulations of Vittori & Verzicco (1998) seem to support the first mechanism.

A first attempt to experimentally investigate vortex structures in an oscillatory boundary layer at moderate values of the Reynolds number was made by Fishler & Brodkey (1991) who suspended tracer particles in a fluid and took high-speed motion pictures of their motions. The experiments were made in a straight, rigid pipe of circular cross-section, where the flow was driven by the simple harmonic motion of a piston. Therefore two parameters controlled the flow characteristics: the Reynolds number R_δ and the Stokes parameter β defined by $\beta = R^*/\delta^*$, where R^* is the pipe radius. The flat wall case is recovered when β tends to infinity. The results of Fishler & Brodkey (1991) showed that in the intermittently turbulent regime, large vortex structures occurred randomly in space, but their time development was deterministic. The largest turbulent events were detected near or subsequent to the beginning of the decelerating phases, and the observed vortex structures were similar to those of steady flows such as presented by Corino & Brodkey (1969) and Nychas, Hershey & Brodkey (1973). By visualizing the flow for $\beta = 8.2$ and $R_\delta = 1340$, Fishler & Brodkey (1991) found that the first event of the sequence was a local deceleration, with the fluid near the wall moving slower than the fluid in the same position at a previous time. Immediately after the local deceleration, large inflows towards the wall were observed. This was the local acceleration event, which originated near the outer edge of the wall region and upstream from the retarded region. Simultaneously with or directly after the local acceleration event, the excitation event and the generation of a transverse vortex took place. The excitation event was characterized by random chaotic radial motions throughout the entire wall region. Transverse vortices always occurred simultaneously with the excitation event. Moreover, during the time that the wall region was in an excited state, ejections were observed. The ejection event was characterized by a large amount of radial motion with the fluid simultaneously moving downstream and away from the wall. Ejections were observed to occur at all angles from the wall region, but most of them were observed to be perpendicular to the wall or pointed in the downstream direction. Finally the flow returned to its basic rectilinear motion (sweep event) until the next sequence of events. As previously

pointed out, the coherent turbulent motions described above were observed for fixed values of β and R_δ. However Fishler & Brodkey (1991) determined also how these vortex structures varied with β and R_δ, showing in particular that turbulence tended to disappear when β was increased.

A similar experiment was made by Sarpkaya (1993), who used a different apparatus and, more importantly, investigated lower values of R_δ, thus clearly identifying the dynamics of the observed vortex structures. In particular Sarpkaya (1993) used a long cylindrical body immersed in a sinusoidally oscillating fluid which moved parallel to the cylinder axis. The ratio between the radius R^* of the cylinder and δ^* was large enough ($R^*/\delta^* = 58$) to consider the results obtained to be of significance for the flow over a flat plate. For $R_\delta = 400$, the flow was characterized by the presence of unevenly spaced streaks of tracers which emerged toward the end of each decelerating phase and then completely disappeared during the accelerating phase. These streaks, which were assumed to indicate the presence of streamwise vortices, remained perfectly straight, smooth and parallel with no visible interaction. When the Reynolds number was increased ($420 < R_\delta < 460$), other events took place. The streaks interacted, moving towards each other and growing in amplitude, and then tended to coalesce to form a single streak which became sinuous. Shortly thereafter, the streak began to split into short segments which, in turn, began to lift. Moreover parts of the original pair of streaks acquired larger amplitude and gave rise to 'pockets' (Falco 1991). Finally Sarpkaya (1993) argued the presence of hairpin or horseshoe vortices which, as the velocity of the ambient flow increased, folded back, stretched rapidly and became incoherent structures. When the Reynolds number was further increased to about 460–490, a large number of vortices appeared towards the end of the decelerating phases. Usually these turbulent structures did not survive during the accelerating phases and the flow relaminarized. Further increases of the Reynolds number (490–520) led to more numerous vortex structures which penetrated further into the ambient flow. At higher Reynolds number, turbulence activity spanned over larger times and larger areas, till at values of R_δ around 800 the identification of coherent structures became difficult. Even at values of R_δ as large as 1800 there were still some time intervals in the cycle where the flow was in a transitional state or in a partially developed turbulent state.

At this stage it is worth pointing out that the visualization techniques used by both Fishler & Brodkey (1991) and Sarpkaya (1993) do not allow a complete picture of vortex dynamics. First, as pointed out by Sarpkaya (1993) himself, the results obtained showed coherent structures along a particular plane while it would have been most desirable to have views of the structures in all planes. However, unlike the experiments with synthetic hairpins (see e.g. Acarlar & Smith 1987), the flow structures in an oscillating flow look more irregular and do not necessarily repeat themselves in the same volume of observation. Thus it is nearly impossible to produce experimentally simultaneous views of a given structure in all possible planes. Moreover, flow visualizations at large Reynolds numbers become quite difficult because of the large number of vortex structures and their short lifetime. Secondly, a great deal of caution must be exercised in interpreting the streakline behaviour. An example has been presented by Hama (1962) who showed that streaklines in a tanh-type shear layer velocity profile perturbed by an unamplified travelling sinusoidal-velocity wave may give rise to the roll-up of streaklines as if discrete vortices were present, when in fact no such vortex structures were present.

In the present work the oscillatory flow over a flat wall is reproduced by means of numerical simulations of the Navier–Stokes and continuity equations. As in Blondeaux

& Vittori (1994), Verzicco & Vittori (1996) and Vittori & Verzicco (1998) the wall is not perfectly flat but small imperfections are introduced in the wall profile. In fact, as discussed by Spalart & Baldwin (1988) and Akhavan *et al.* (1991), when a perfectly flat wall is considered, transition can be triggered only by inserting quite large perturbations and for Reynolds numbers larger than those observed in the experimental works. On the other hand, even a quite small waviness can induce the presence of significant perturbations in a range of the Reynolds number for which the disturbed laminar flow is experimentally observed and can generate turbulence when the Reynolds number is larger than a critical value, which fairly well agrees with experimental observations (Verzicco & Vittori 1996; Vittori & Verzicco 1998). Therefore both the disturbed laminar and the intermittently turbulent regimes are simulated.

The results concerning the critical values of the Reynolds number for which the disturbed laminar regime and the intermittently turbulent regime appear are presented in Vittori & Verzicco (1998), where the average flow characteristics are also described. Hence, no further investigation of these quantities is made herein. Rather, we investigate the vortex structures which appear in both the disturbed laminar and intermittently turbulent regimes, in an attempt to isolate the basic unit flow, to study its morphology and dynamics and to provide some physical insight into the mechanisms controlling momentum, mass and heat transfer in oscillatory boundary layers. Vortex structures are identified by visualizing the flow and analysing the vorticity field. In addition, since the analysis of the isovorticity surfaces may be considered not fully adequate to detect vortices, we also use the definition of vortex structures proposed by Jeong & Hussain (1995) and we visualize the regions with two negative eigenvalues of the symmetric tensor $\boldsymbol{D}^2 + \boldsymbol{\Omega}^2$, where $\boldsymbol{D}$ and $\boldsymbol{\Omega}$ denote the symmetric and antisymmetric parts of the velocity gradient tensor respectively. As discussed by Jeong & Hussain (1995), this definition captures the pressure minimum in a plane perpendicular to the vortex axis at high Reynolds numbers and also accurately defines vortex cores at low Reynolds numbers, unlike a pressure minimum criterion which sometimes is used as an intuitive indicator of a vortex. The above approach has revealed the same vortex structures identified by means of flow visualizations and the analysis of the isovorticity surfaces.

In the disturbed laminar regime, the results obtained and in particular the structure of the simulated coherent vortices depend on the characteristics of the wall imperfections. Significant perturbations of the basic flow appear only when a two-dimensional wall waviness is present, the wavenumber of which is close to that predicted by Blondeaux & Vittori (1994). Moreover, by increasing the amplitude of the wall waviness the critical value of the Reynolds number giving rise to the intermittently turbulent regime can be decreased. On the other hand, in the intermittently turbulent regime, turbulence is found to be independent of the characteristics of wall imperfections and, once present, turbulence is self-sustaining. The results obtained show that the coherent vortex structures appearing in the intermittently turbulent regime are similar to those detected in steady boundary layers. However the sequence of events generating turbulence does not take place randomly in time but is characterized by a repetition time scale which is about half the period of fluid oscillations. In particular low-speed streaks, which start to appear towards the end of the accelerating phases, have been observed. Later, during the decelerating phases, the low-speed streaks oscillate, twist and eventually break generating small-scale vortices which later, during the accelerating phases, damp because of viscous effects. Moreover, the analysis of the vorticity field in the region far from the wall has shown the existence of a sequence of short

streamwise vortices of alternating circulation pumping low-speed fluid far from the wall (Sendstad & Moin 1992). Finally, the present findings suggest that turbulence in an oscillating boundary layer is generated and sustained by a streak instability mechanism; no evidence of well-defined parent vortex structures spawning offspring vortices is found. Further investigations need to be made to identify the characteristics of the instability mechanism.

2. The problem and the numerical approach

As pointed out in the Introduction, we study the boundary layer generated close to a wall by an oscillating pressure gradient which, outside the boundary layer, is described by

$$\frac{\partial P^*}{\partial x_1^*} = -\rho^* U_0^* \omega^* \sin(\omega^* t^*), \quad \frac{\partial P^*}{\partial x_2^*} = 0, \quad \frac{\partial P^*}{\partial x_3^*} = 0, \tag{1}$$

where x_1^*, x_2^* and x_3^* indicate streamwise, vertical (or cross-stream) and spanwise coordinates respectively and the average wall location coincides with the (x_1^*, x_3^*)-plane. Hereinafter an asterisk is used to denote dimensional quantities. In (1) ρ^* is the constant density of the fluid, and U_0^* and ω^* are the amplitude and the angular frequency of fluid velocity oscillations induced by (1) far from the wall.

The wall is not perfectly flat but characterized by a small waviness and its profile η^* is given by the superposition of sinusoidal components

$$x_2^* = \epsilon^* \eta(x_1^*, x_3^*) = \epsilon^* \sum_{n=1}^{N} a_n \cos(\alpha_n^* x_1^* + \gamma_n^* x_3^* + \varphi_n), \tag{2}$$

where $\epsilon^* a_n$ denotes the amplitude of the nth component which is characterized by wavenumbers α_n^* and γ_n^* in the x_1^*- and x_3^*-directions respectively and by a phase φ_n.

Use is made of dimensionless variables defined as

$$\left.\begin{aligned} t = t^* \omega^*, \quad \boldsymbol{x} = (x_1, x_2, x_3) = \frac{(x_1^*, x_2^*, x_3^*)}{\delta^*}, \\ \boldsymbol{u} = (u_1, u_2, u_3) = \frac{(u_1^*, u_2^*, u_3^*)}{U_0^*}, \quad p = \frac{p^*}{\rho^* (U_0^*)^2}. \end{aligned}\right\} \tag{3}$$

In (3) t^* is time, u_1^*, u_2^*, u_3^* are the fluid velocity components along the x_1^*-, x_2^*- and x_3^*-directions respectively and δ^* is the conventional thickness of the viscous boundary layer close to the wall defined as $\sqrt{2\nu^*/\omega^*}$, ν^* being the kinematic viscosity of the fluid.

The problem is thus posed by the Navier–Stokes and continuity equations:

$$\frac{\partial \boldsymbol{u}}{\partial t} + \frac{R_\delta}{2} \nabla \cdot (\boldsymbol{u}\boldsymbol{u}) = -\frac{R_\delta}{2} \nabla p - \boldsymbol{i}_{x_1} \sin(t) + \tfrac{1}{2} \nabla^2 \boldsymbol{u}, \tag{4}$$

$$\nabla \cdot \boldsymbol{u} = 0, \tag{5}$$

where $\boldsymbol{i}_{x_1}$ is the unit vector in the streamwise direction and $R_\delta = U_0^* \delta^* / \nu^*$.

The governing equations are solved numerically in a computational domain of dimensions L_{x_1}, L_{x_2} and L_{x_3} in the streamwise, cross-stream and spanwise directions respectively.

At the wall the no-slip condition is enforced:

$$(u_1, u_2, u_3) = 0 \quad \text{at} \quad x_2 = \epsilon \eta(x_1, x_3). \tag{6}$$

Having assumed the amplitude of the wall waviness to be much smaller than the thickness of the laminar boundary layer ($\epsilon = \epsilon^*/\delta^* \ll 1$), boundary condition (6) can be approximated as

$$(u_1, u_2, u_3) = -\epsilon\eta(x_1, x_3)\frac{\partial}{\partial x_2}(u_1, u_2, u_3) + 0(\epsilon^2) \quad \text{at} \quad x_2 = 0. \tag{7}$$

Note that (7) is an approximation of the boundary condition (6) within the accuracy of the numerical method employed to solve (4)–(5). The numerical scheme is second-order accurate in space and in all the simulations ϵ has been taken to be smaller than the first computational step in the x_2-direction. At large distances from the wall the flow field should tend to $(-U_0^* \cos\omega^* t, 0, 0)$. Hence, at $x_2 = L_{x_2}$, where L_{x_2} is much larger than one, a symmetry condition is imposed:

$$\frac{\partial}{\partial x_2}(u_1, u_3) = 0, \quad u_2 = 0, \tag{8}$$

which is equivalent to requiring the vanishing of tangential stresses far from the wall and imposing that the flow field far from the wall tends to $(-U_0^* \cos\omega^* t^*, 0, 0)$. Moreover, the turbulent flow is assumed to be homogeneous in the streamwise and spanwise directions and periodic boundary conditions are thus forced along the x_1- and x_3-axes.

The numerical method solves the problem in primitive variables using standard centred second-order finite difference approximations of the spatial derivatives, while the time-advancement of Navier–Stokes equations employs a fractional-step method extensively described by Kim & Moin (1985), Orlandi (1989) and Rai & Moin (1991). The non-solenoidal intermediate velocity field is evaluated by means of a third order Runge–Kutta scheme to discretize convective terms together with a Crank–Nicolson scheme for the diffusive terms. The implicit treatment of the viscous terms would require the inversion of large sparse matrices which are reduced to three tridiagonal matrices by a factorization procedure with an error of order $(\Delta t)^3$ (Beam & Warming 1976). Then, by forcing the continuity equation (5), a Poisson equation for the pressure field is obtained which is readily solved by taking advantage of the imposed periodicity in the x_1- and x_3-directions. More details on the numerical approach can be found in Vittori & Verzicco (1998) where a comparison is also made between the numerical results and some analytical solutions which hold for small or moderate values of the Reynolds number R_δ (Blondeaux 1990; Vittori 1992). The satisfactory agreement found by Vittori & Verzicco (1998) supports the reliability and accuracy of the numerical approach.

The use of periodic boundary conditions in the homogeneous directions is justified if the computational box is large enough to include the largest eddies in the flow.

The works by Blondeaux & Seminara (1979), Akhavan *et al.* (1991), Wu (1992), Blondeaux & Vittori (1994) and Vittori & Verzicco (1998) suggest that the flow structures, which tend to appear when transition to turbulence takes place, are characterized by a length in the streamwise direction equal to about $12.56\delta^*$ and a width in the spanwise direction of about $6.28\delta^*$. Then, these vortex structures break, originating smaller vortices which dissipate because of viscous effects. Since, as in Jimenez & Moin (1991), the goal here is to isolate the basic flow unit and to study its morphology and dynamics, we aimed to keep the size of the computational box as small as possible to reproduce the process of turbulence generation. On the basis of preliminary numerical experiments, a set of runs has been made with a box size equal to $L^*_{x_1} = 25.13\delta^*$ and $L^*_{x_3} = 12.57\delta^*$ in the streamwise and spanwise

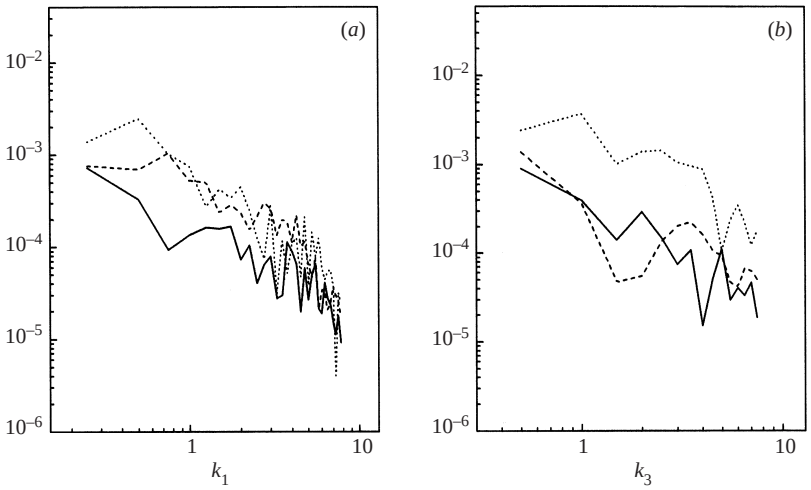

FIGURE 1. Instantaneous spatial velocity power spectra, along the (*a*) streamwise and (*b*) spanwise directions at $x_2 = 2.5$, $t = 42.52\pi$ and $R_\delta = 800$. The streamwise spectrum is averaged in the spanwise direction and the spanwise spectrum is averaged in the streamwise direction (dotted line, streamwise velocity component; solid line, vertical velocity component; dashed line, spanwise velocity component).

directions respectively. For this box size, turbulence is generated and maintained for Reynolds numbers in fair agreement with experimental values. Moreover the average quantities, like velocity, turbulence energy and Reynolds stresses, agree fairly well with experimental measurements (see Vittori & Verzicco 1998). For all the simulations described in the present paper, the dimensionless vertical size of the computational box has been fixed equal to $L^*_{x_2} = 25.13\delta^*$. At such distances from the wall significant values of vorticity have never been detected. An estimate of the box size in terms of wall units can be obtained using the time-averaged value of the shear velocity predicted on the basis of Stokes' (1855) solution. Indeed, experimental data show that the wall shear stress in the intermittently turbulent regime has values not much different from those characterizing the laminar solution. In the Reynolds number range investigated here, it turns out that the length of the computational box falls between 450 and 820 wall units depending on the Reynolds number, while its width varies between 225 and 410 wall units. Such values are similar to those used by Jimenez & Moin (1991) to study vortex structures in the wall layer for a steady flow.

In the computational box, $64 \times 32 \times 64$ grid points have been used in the streamwise, spanwise and vertical directions respectively. The mesh is uniform in the streamwise and spanwise directions while in the vertical one a non-uniform mesh has been used to cluster the grid points in the vicinity of the wall where gradients are expected to be stronger. An example of the instantaneous streamwise and spanwise power spectra is shown in figure 1 at the phase of the cycle when turbulence appears explosively and the smallest vortices are generated. The plots of figure 1 are for $R_\delta = 800$ and show an acceptable drop-off at high frequencies, confirming that the smallest scales are adequately resolved.

However, the results obtained show that the box is too small to adequately represent all turbulence characteristics. Indeed, after averaging in the x_1- and/or x_3-directions parallel to the wall, the computed quantities display a stochastic and intermittent behaviour which is due to the limited size of the box in comparison with the

largest vortex structures. The plots of figure 1, which show the instantaneous Fourier transforms of the velocity component in the streamwise direction averaged in the spanwise direction and vice versa, are examples of such behaviour. A similar problem was faced by Jimenez & Moin (1991), who circumvented it by performing the time average of spatially averaged quantities. In the present work a phase-average value could be computed. However in the Reynolds number range investigated, turbulence appears at different instants within the cycle and a phase-average procedure would have implied averaging flow fields with different characteristics. Hence, in the following, no phase-averaging is used, unless justified and explicitly specified.

To check that the limited size of the box does not affect the dynamics of the observed vortex structures, some of the runs have have been repeated with larger values of $L^*_{x_1}$ and $L^*_{x_3}$. In particular for $R_\delta = 800$ results have been obtained with $L^*_{x_1} = 50.27\delta^*$ and $L^*_{x_3} = 25.14\delta^*$ such that the length and width of the computational box are roughly 1290 and 640 wall units respectively. For the runs with the large computational box, the number of grid points was more than doubled both in the streamwise and spanwise directions and $192\times96\times64$ grid points were used in the streamwise, spanwise and vertical directions respectively. Figure 2 shows that the instantaneous two-point spatial autocorrelation functions for the velocity field tend to vanish both for the small and large boxes but the small box is not large enough for distant points to be completely uncorrelated. In figure 2, the phases of the cycle when low-speed streaks start to break up are considered and the autocorrelation functions are evaluated at $x_2 = 2.5$. Therefore, as in Jimenez & Moin (1991), the small computational box cannot allow an accurate prediction of the high-order statistical quantities, even though it can be used to isolate the basic process generating turbulence. On the other hand, the instantaneous autocorrelation functions for the large box are almost zero at half the computational domain and in this case the numerical predictions can be used to investigate turbulence structure both near and far from the wall.

To support the reliability of the computations, the numerical results have been compared with available experimental data. Accurate measurements are described in Jensen, Sumer & Fredsoe (1989). In particular, we have chosen to compare our numerical results with the data of tests nos. 5, 6 and 7 which are characterized by sufficiently high Reynolds numbers ($R_\delta \approx 740, 990, 1120$) to be considered in the intermittently turbulent regime but not so large as to require high computational costs. Here, attention is focused on turbulence characteristics. Figures 3 and 4, where the near-wall turbulent intensities are plotted at different phases of the cycle, show a fair agreement between the computed and measured values. Figure 5, where the predicted and measured time developments of the wall shear stress are plotted, further supports the numerical procedure. It is worth pointing out that the experimental data of figure 5 represent phase-averaged values while the numerical predictions are just one realization of the phenomenon. The numerical predictions shown in figure 5(a) are characterized by significant differences from cycle to cycle which are due to the proximity of the Reynolds number to the critical value.

3. Discussion of the results

As pointed out in the introduction, in the oscillatory flow over a flat wall four regimes can be identified: (i) the laminar regime; (ii) a disturbed laminar regime, where small-amplitude perturbations appear superimposed on the Stokes flow; (iii) an intermittently turbulent regime, where bursts of turbulence appear explosively at the end of the accelerating phases and are sustained during the decelerating phases

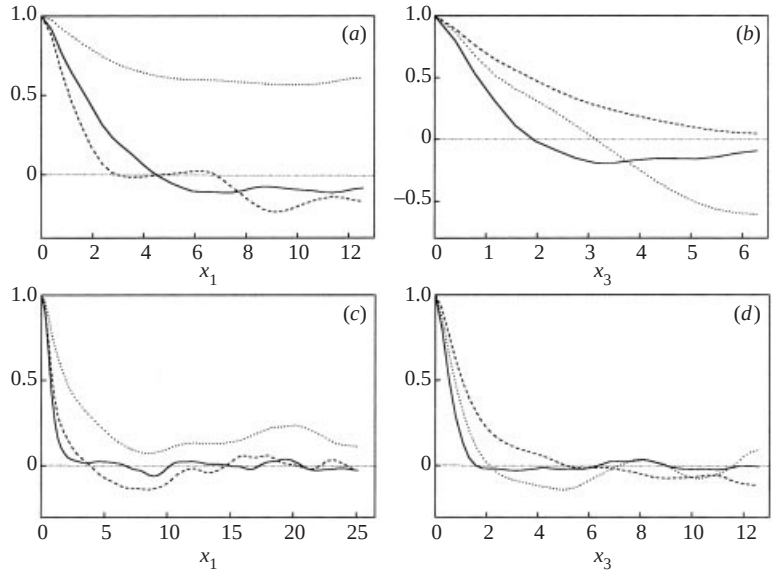

FIGURE 2. Two-point spatial autocorrelation functions along (*a*) the streamwise direction and (*b*) the spanwise direction (small box, $t = 42.52\pi$); (*c*) the streamwise direction and (*d*) the spanwise direction (large box, $t = 43.04\pi$) at $x_2 = 2.5$ and $R_\delta = 800$ (dotted line, streamwise velocity component; solid line, vertical velocity component; dashed line, spanwise velocity component). The autocorrelation function along the streamwise direction is averaged in the spanwise direction and vice versa. In both cases the plots span half the computational box domain.

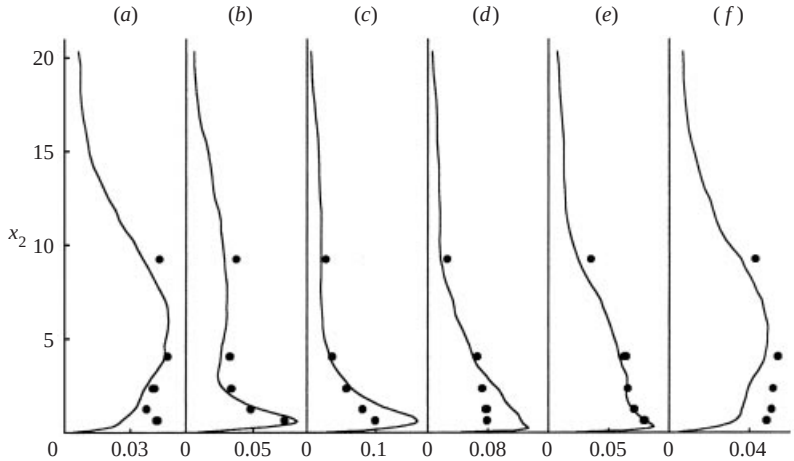

FIGURE 3. Comparison between computed and measured r.m.s. values of the streamwise velocity component for $R_\delta \approx 990$ (Test no. 6 of Jensen *et al.* 1989). Phases of the cycle (*a*) 95°, (*b*) 130°, (*c*) 163°, (*d*) 17°, (*e*) 50°, (*f*) 85° (dots, experimental data; solid line, numerical predictions).

of the cycle; (iv) a fully developed turbulent regime characterized by the presence of turbulence throughout the whole cycle.

Here, computations are made to gain qualitative and quantitative information on the vortex structures characterizing the flow for moderate values of the Reynolds number, i.e. for R_δ falling in the first three regimes, and to better understand the role of coherent structures in the transition from the laminar to the disturbed laminar

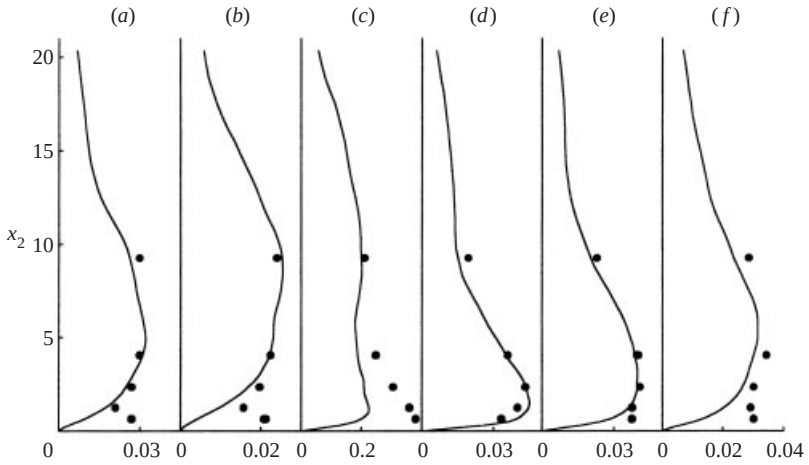

FIGURE 4. Comparison between computed and measured r.m.s. values of the vertical velocity component for $R_\delta \approx 990$ (Test no. 6 of Jensen *et al.* 1989). Phases of the cycle (*a*) 95°, (*b*) 130°, (*c*) 163°, (*d*) 171°, (*e*) 50°, (*f*) 85° (dots, experimental data; solid line, numerical predictions).

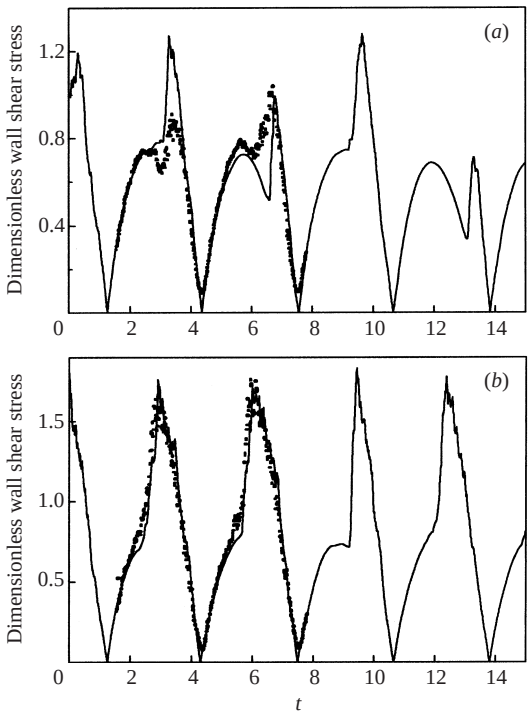

FIGURE 5. Comparison between computed and measured (Jensen *et al.* 1989) wall shear stress. (*a*) $R_\delta \approx 740$ (test no. 5), (*b*) $R_\delta \approx 1120$ (test no. 7) (dots, experimental data; solid line, numerical predictions).

regime and from the disturbed laminar to the intermittently turbulent regime. No results are available in the fully turbulent regime, because the computational costs prohibit numerical simulations for large values of the Reynolds number.

Computed visualizations of the trajectories of passive tracers are used to obtain preliminary information on the vorticity field. Even though the analysis of the

trajectories of passive tracers cannot be used to definitely identify vortex structures, flow visualizations by means of marker trajectories have been made to allow a direct comparison between the numerical simulations and the experimental data of other authors and in particular of Sarpkaya (1993). There are no well-established and accurate quantitative results on turbulence structure in oscillatory boundary layers at transitional and moderate values of the Reynolds number and a comparison of the numerical results with previous experimental flow visualizations is necessary to provide further support to the numerical procedure. In particular two techniques are used. In the first one, tracers are released along a line at a fixed time interval Δt and then their motions are followed. This technique, which simulates the hydrogen bubble technique, not only allows a large portion of the flow to be visualized, but can also be used to obtain an immediate estimate of the velocity distribution along the line of emission. In the second technique, numerical dye (tracer) is introduced at a fixed time along a plane parallel to the wall thus following the experimental procedure used by Sarpkaya (1993). Pictures taken at subsequent times allow the dye motions to be identified and the presence of coherent vortices inferred.

Having obtained a qualitative picture of the flow structure, a quantitative investigation is made of the coherent vortices, from velocity, pressure and vorticity fields in the three-dimensional space and time. In particular, using the definition of a vortex introduced by Jeong & Hussain (1995) for an incompressible flow, we identify coherent vortex structures as connected regions with two negative eigenvalues of the symmetric tensor $\boldsymbol{D}^2 + \boldsymbol{\Omega}^2$ ($\boldsymbol{D}$ and $\boldsymbol{\Omega}$ are the symmetric and antisymmetric parts of the velocity gradient tensor respectively).

3.1. *The disturbed laminar regime*

For small values of the Reynolds number, vorticity has only the spanwise component associated with the Stokes flow, except for the presence of small perturbations induced by the presence of wall imperfections. However these perturbations remain very small throughout the cycle and are proportional to ϵ. The analysis of the tracers does not show any relevant vortex structure and the flow regime can be defined as laminar. The flow remains laminar up to R_δ equal to about 100.

Then, for larger values of the Reynolds number, the resonance mechanism discussed by Blondeaux & Vittori (1994) starts to appear and perturbations develop which are forced by wall imperfections but are characterized by amplitudes which are much larger than ϵ. Hence, when R_δ is larger than 100, the 'disturbed laminar regime' occurs. However the process is continuous and the strength of the flow perturbations which are detected becomes relevant only when the Reynolds number is significantly larger than 100.

To investigate the vortex structures which appear when resonance takes place and to highlight the major role played by wall imperfections in triggering the growth of flow perturbations when the Reynolds number falls in the disturbed laminar regime, three wall configurations have been considered. The first one (denoted A) is that used by Vittori & Verzicco (1998). In particular the wall profile A has two harmonic components ($N = 2$). The first one is two-dimensional, i.e. it does not depend on x_3, and has the wavenumber characteristic of the most unstable two-dimensional disturbance according to Blondeaux & Seminara (1979) ($\alpha_1 = 0.5$, $\gamma_1 = 0$). The second component has been chosen with the same spanwise spatial periodicity as that of the three-dimensional perturbations which Akhavan *et al.* (1991) showed to have the maximum growth rate when interacting with a pre-existing finite-amplitude two-dimensional wave ($\alpha_2 = 0$, $\gamma_2 = 1$). Moreover $a_1 = 1$, $a_2 = 0.1$ and $\varphi_1 = \varphi_2 = 0$.

This set of parameters has been chosen since the analyses of Blondeaux & Vittori (1994) and Akhavan *et al.* (1991) show that it is able to induce resonance and trigger turbulence. Finally the value of ϵ has been set equal to 0.005, which is typical of the imperfections for a mirror-shine smooth wall. The second wall configuration (denoted B) is the sum of two oblique waves ($N = 2$), which are symmetric with respect to the flow direction and characterized by streamwise and spanwise wavenumbers equal to $(\alpha_1, \gamma_1) = (0.5, 1)$ and $(\alpha_2, \gamma_2) = (0.5, -1)$ respectively. Moreover $a_1 = a_2 = 0.5$ and $\varphi_1 = \varphi_2 = 0$. In this case the amplitude ϵ is equal to that of configuration A ($\epsilon = 0.005$). For such values of the parameters no resonance is expected to take place (see figure 4 of Blondeaux & Vittori 1994). The third wall configuration (wall C) is obtained setting $N = 3$ and ϵ still equal to 0.005. Moreover we fixed ($\alpha_1 = 1,\ \gamma_1 = 0$), ($\alpha_2 = 0.5,\ \gamma_2 = 0.866$) and ($\alpha_3 = 0.5,\ \gamma_3 = -0.866$) with $a_1 = 0.136$, $a_2 = a_3 = 0.5$. In this case only, the width L_{x_3} of the computational box has been set equal to 14.51. These values have been chosen in an attempt to force a disturbance which should be highly unstable and show an explosive growth according to the analysis by Wu (1992) and Wu, Lee & Cowley (1993). For flows in the disturbed laminar regime, the simulations were carried out till $t = 12\pi$, i.e. 6 cycles.

The presence of resonance for R_δ larger than 100 is supported by flow visualizations. In fact, looking at the trajectories of tracers uniformly released at $t = 10\pi$ along a plane parallel to the wall located at $x_2 = 0.2$ for $R_\delta = 500$ and wall A, it is possible to observe the formation of spanwise bands of tracers travelling in the streamwise direction. The geometry and spacing of these bands suggest the presence of two-dimensional perturbations with a streamwise wavelength equal to about $12.6\delta^*$, i.e. the wavelength of the wall imperfections (see figure 6). However the presence of the wall waviness alone cannot explain such large-amplitude waves which indeed are triggered by wall imperfections but are then amplified by the resonance mechanism described by Blondeaux & Vittori (1994).

Figure 7 shows the spanwise component $\tilde{\Omega}_3$ of the vorticity field at $t = 11\pi$, after the subtraction of the vorticity $\overline{\Omega}_3$ averaged over the plane (x_1, x_3) ($\tilde{\Omega}_3 = \Omega_3 - \overline{\Omega}_3$), for $R_\delta = 500$ and wall A. The mean vorticity is removed to take away the vorticity associated with the basic flow and to highlight the vorticity associated with the perturbations. Well-developed spanwise vortices can be detected, the strength of which is significantly larger than ϵ, which is the order of magnitude of the expected vorticity perturbations induced by wall imperfections in the absence of any resonance phenomenon. Further support to the analysis of Blondeaux & Vittori (1994) comes from the observation that these vortices grow when resonance takes places, because of an energy supply from the basic flow, and then they decay due to viscous effects when resonance is no longer active. This result comes from an analysis of figure 8 where the vertically integrated specific vorticity $\mathcal{O}$ and its time derivative are plotted versus time:

$$\mathcal{O} = \frac{1}{L_{x_1} L_{x_3}} \int_0^{L_{x_1}} \int_0^{L_{x_2}} \int_0^{L_{x_3}} \sqrt{\Omega_1^2 + \Omega_2^2 + \tilde{\Omega}_3^2}\, \mathrm{d}x_1\, \mathrm{d}x_2\, \mathrm{d}x_3. \tag{9}$$

The function $\mathcal{O}$ is characterized by a rapid growth at $t \sim 0.5n\pi$ which correspond to the resonant phases predicted by Blondeaux & Vittori (1994) (see figure 5 of their paper). Moreover, once created, vorticity does not disappear suddenly but is damped by viscous effects as shown by Blondeaux & Vittori (1994) who investigated the passage through resonance (see figure 8 of their paper).

The present results also support Akhavan *et al.*'s (1991) findings; the analysis of the trajectories of the tracers for longer times has shown that three-dimensional

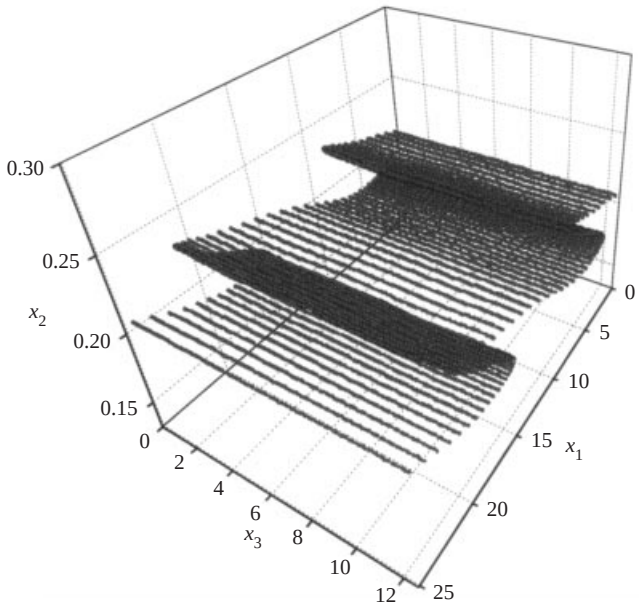

FIGURE 6. Visualization at $t = 10.80\pi$ of markers uniformly released at $t = 10\pi$ and $x_2 = 0.2$ ($R_\delta = 500$ and wall A).

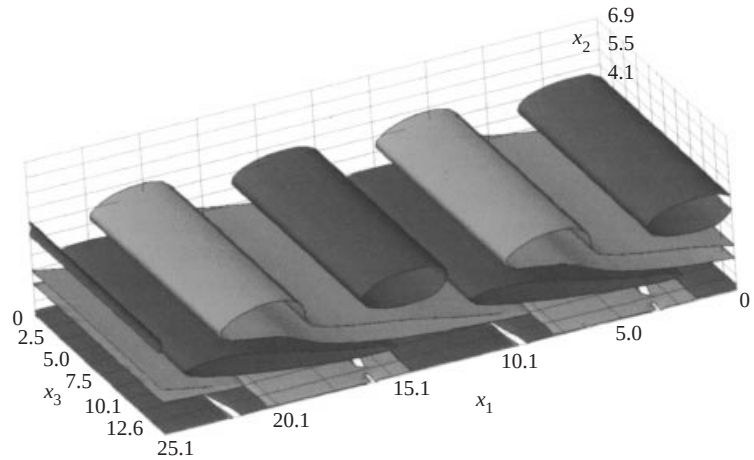

FIGURE 7. Spanwise vorticity component $\tilde{\Omega}_3$ at $t = 11\pi$ for $R_\delta = 500$ and wall A. Isosurface for $|\tilde{\Omega}_3| = 0.1$ (light surface, positive values; dark surface, negative values).

perturbations slowly grow as predicted by Akhavan *et al.* (1991). In fact figure 9 shows that for longer times the markers tend to assume a wavy configuration in the spanwise direction (compare figure 6 with figure 9). We remind the reader that for $R_\delta = 500$ the amplification rate of the spanwise perturbations predicted by Akhavan *et al.* (1991) is very small and this explains why it takes a long time to see a significant spanwise waviness in the marker distribution. It is also worth pointing out that notwithstanding the growth of three-dimensional perturbations, which is inferred by the analysis of the trajectories of the tracers, no significant three-dimensional vortex structure can be isolated when looking at the vorticity field up to $t = 12\pi$.

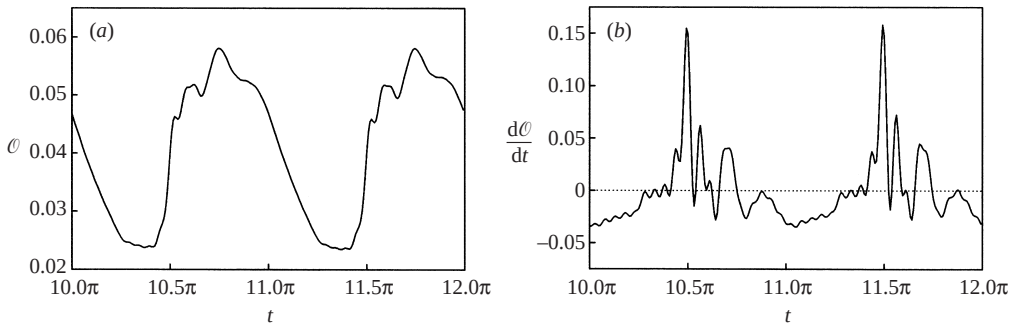

FIGURE 8. (*a*) Specific vorticity $\mathcal{O}$; (*b*) time derivative of the specific vorticity $\mathcal{O}$ ($R_\delta = 500$ and wall A).

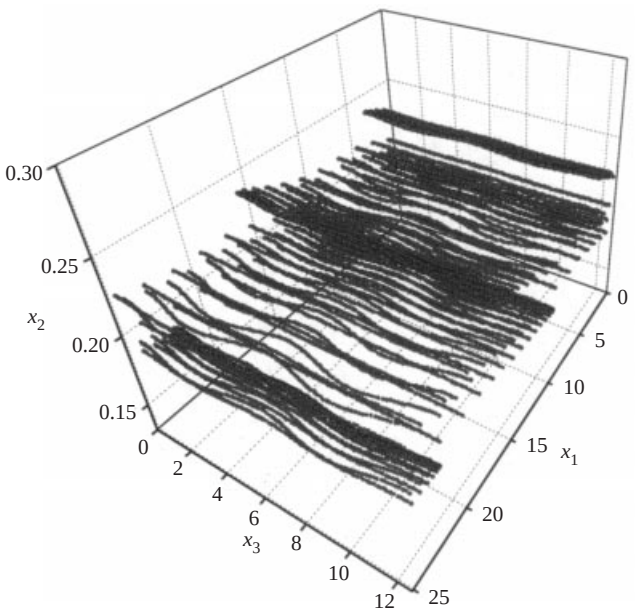

FIGURE 9. Visualization at $t = 11.47\pi$ of markers uniformly released at $t = 10\pi$ and $x_2 = 0.2$ ($R_\delta = 500$ and wall A).

On the other hand, for wall B, the values of $\tilde{\Omega}_3$ are of order ϵ and it can be inferred that no resonance takes place. Moreover, for wall B, notwithstanding the presence of a wall waviness as large as that of wall A, no significant pattern in the trajectories of the tracers is observed.

The simulation carried out for $R_\delta = 500$ and wall C does not show any growth of significant flow perturbations either, thus indicating that the mechanism investigated by Wu (1992) and Wu *et al.* (1993) does not operate for this value of the Reynolds number. This finding is not surprising since the analyses carried out by Wu (1992) and Wu *et al.* (1993) hold only for R_δ tending to infinity.

Similar results are found for other values of R_δ falling in the disturbed laminar regime. In particular numerical simulations have been made for R_δ equal to 300 and 400, showing that the resonance mechanism becomes weaker when the Reynolds number is decreased. Even though in the disturbed laminar regime the fluid motion

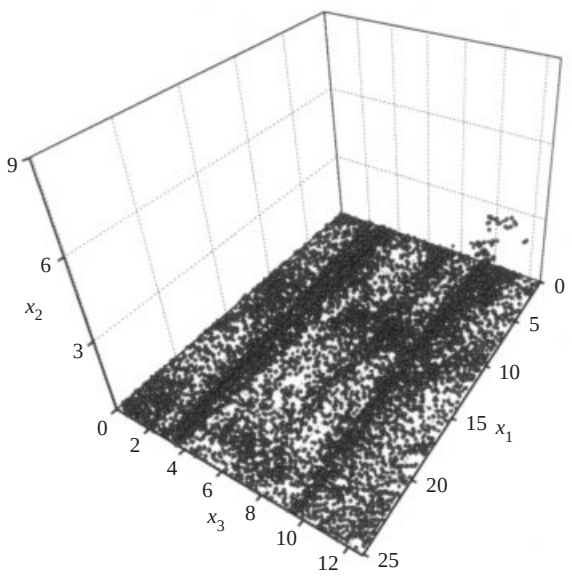

FIGURE 10. Visualization at $t = 24.98\pi$ of markers uniformly released at $t = 24.5\pi$ and $x_2 = 0.1$ ($R_\delta = 500$ and wall D).

is still coherent and no turbulence is detected, the flow significantly differs from that predicted by Stokes when appropriate wall imperfections are introduced.

The above numerical results seem to disagree with the experimental observations of Sarpkaya (1993) who observed coherent three-dimensional vortex structures for R_δ as small as 400 and turbulence for R_δ around 500. In particular for $R_\delta = 400$ Sarpkaya (1993), looking at patterns formed by dye uniformly released on the cylinder surface, observed one or more unevenly spaced low-speed streaks which remained perfectly straight, smooth and parallel. For larger values of R_δ but still smaller than 500, the streaks became sinuous, interacted with each other and eventually broke up, generating turbulence. This discrepancy between the numerical simulations and the experimental data may be ascribed to the different amplitude of the external disturbances present in the experimental apparatus with respect to the perturbations induced by wall imperfections. Indeed, a numerical simulation carried out for $R_\delta = 500$ and wall D, which is equal to wall A but with an amplitude ϵ which is an order of magnitude larger ($\epsilon = 0.04$), shows results which qualitatively agree with those described by Sarpkaya (1993) and fall in the intermittently turbulent regime. Flow visualizations performed following the motion of a uniform layer of tracers released parallel to the wall show the formation of streamwise streaks which remain straight, smooth and parallel for a long time (see figure 10) and then split into short segments which in turn are lifted and break up. It is worth recalling that $\epsilon = 0.04$ corresponds to imperfections of a wall which is still flat from a macroscopic point of view.

Since the simulations provide the velocity and pressure fields in space and time, it would seem appropriate to analyse in more detail the vortex structures characterizing the flow at relatively low Reynolds numbers. However, as previously described, in this range of R_δ the results and in particular the simulated vortex structures depend on the characteristics of wall imperfections. To realize this, it is sufficient to compare figure 7 with figure 11, where the spanwise vorticity component is plotted for the same Reynolds number and the same wall configuration but for different values of the

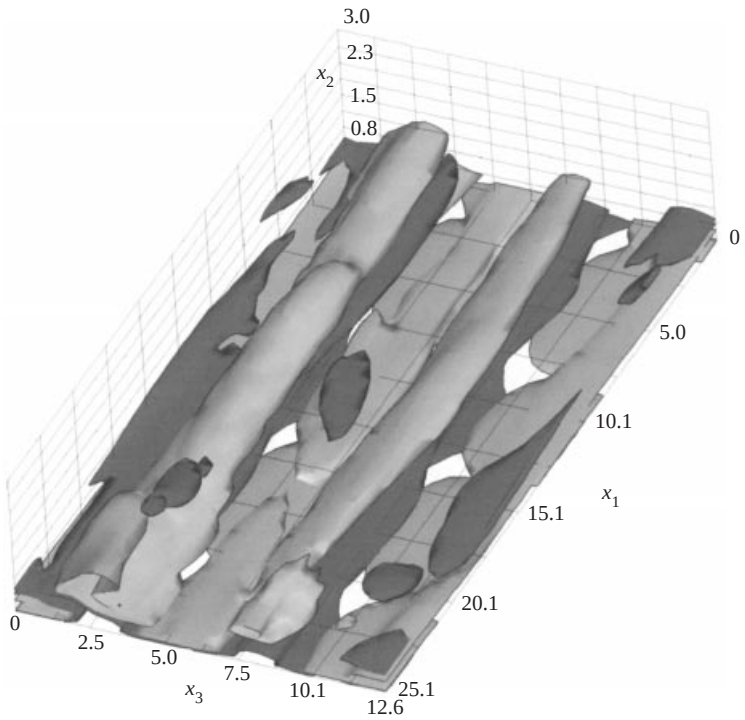

FIGURE 11. Spanwise vorticity component $\tilde{\Omega}_3$ at $t = 11\pi$ for $R_\delta = 500$ and wall D. Isosurface for $|\tilde{\Omega}_3| = 0.21$ (light surface, positive values; dark surface, negative values).

amplitude ϵ of wall imperfections. In figure 7, which shows the results for $\epsilon = 0.005$, spanwise vortices can be recognized, while in figure 11, where ϵ is equal to 0.04, the vorticity field is characterized by streamwise vortex structures. Moreover, an analysis of the velocity field shows that for wall A the flow falls in the disturbed laminar regime while for wall D it falls in the intermittently turbulent regime.

A detailed analysis of the velocity and vorticity fields is postponed to the following section, where larger values of the Reynolds number are considered and the intermittently turbulent regime takes place. In this regime the vortex structures which appear and the characteristics of turbulence do not depend on the form and amplitude of wall imperfections, which are necessary only to trigger transition and can then be removed, once a statistically steady state is reached, without affecting the statistical properties of the flow field.

3.2. *The intermittently turbulent regime*

3.2.1. *Flow visualizations*

The results by Vittori & Verzicco (1998) show that for wall A, the transition from the disturbed laminar regime to the intermittently turbulent regime takes place when R_δ is about 550. Moreover a preliminary set of runs has shown that for R_δ larger than 550, wall imperfections can be removed, once the flow has attained a periodic state, without affecting the average characteristics of velocity and vorticity fields.

Hence, let us start by looking at the results obtained for $R_\delta = 800$ and wall A. Of course the flow does not repeat exactly every half a cycle; however for the case described above and for all the results described in the following, enough cycles

(25 cycles) have been simulated to give some confidence that the features discussed in the paper are representative of the events taking place in the computational box. The flow visualizations allow a sequence of events to be identified similar to those detected in steady wall turbulence. An example of the results is shown in figure 12 where the trajectories of tracers released from a single line at fixed time interval are displayed. In these pictures the line of emission is located parallel to the plate and normal to the flow, which is in the positive direction of x_1. The distance d^* of the line of emission from the wall is equal to $0.1\delta^*$. Generally speaking, in the laboratory experiments performed in steady boundary layers or in closed ducts, the wire (line) shedding hydrogen bubbles (tracers) is located at a distance from the wall which is usually measured in terms of the viscous length ν^*/u_τ^* (u_τ^* being the shear velocity). In the present simulations the shear velocity u_τ^* changes with time, hence the value of the ratio $d^*/(\nu^*/u_\tau^*)$ also changes with time. Thus it appears more appropriate to scale d^* with δ^*. To provide the order of magnitude of the distance from the wall in terms of the viscous length ν^*/u_τ^* we have computed the ratio $\delta^*/(\nu^*/\overline{u_\tau^*})$ where an overbar denotes the average over the cycle. For $R_\delta = 800$, $\delta^*/(\nu^*/\overline{u_\tau^*})$ is found to be equal to about 24, hence the tracers are released within the viscous sublayer at approximately $2.4\nu^*/\overline{u_\tau^*}$.

Towards the end of the accelerating phase and in the early stages of flow deceleration, the analysis of the tracer motions shows the existence of a spanwise distribution of alternating zones of high- and low-speed fluid which develop close to the wall (see figure 12*a*). Moreover, flow visualizations made by releasing a uniform layer of passive tracers at $t = 41.5\pi$ and $x_2 = 0.1$ show that these large spanwise variations in the streamwise velocity component are correlated with spanwise-periodic variations of the spanwise velocity component which tends to create streamwise streaks of high tracer concentration similar to the dye patterns observed by Sarpkaya (1993). This clearly appears when the external flow starts to decelerate (see figure 13). As already pointed out, the streaks form at a rather pronounced spanwise spacing, which remains almost constant when the line of emission is moved in the vertical direction.

Streamwise filaments of low-speed fluid (streaks) with a fairly uniform transverse spacing were first observed in the steady case by Ferrell, Richardson & Beatty (1955) and concurrently by Hama (see Corrsin 1957). A subsequent systematic investigation of the low-speed streak phenomena by Runstadler, Kline & Reynolds (1963) quantified some of their characteristics. Since these pioneering works, low-speed streaks have been investigated by many authors and they are now considered ubiquitous features of turbulent boundary layers. Similar structures have also been observed more recently by Sarpkaya (1993) in an oscillatory boundary layer. One of the main differences between the structures observed in the Stokes layer and those in the steady boundary layer is that the former take place at a particular phase of the cycle, while in steady boundary layers low-speed streaks are randomly observed in time. Here, for $R_\delta = 800$, it has been observed that low-speed streaks start to appear toward the end of the accelerating phases, as observed in the experiments by Fishler & Brodkey (1991), and survive till the end of the decelerating phases, even though in the final period of their life they oscillate and twist. In particular they tend to move toward each other, to coalesce and to form single streaks which become sinuous (see figure 12*b*). Shortly thereafter, the streaks begin to split into short segments which, in turn, are lifted. As a consequence, the markers are spread into the upper layers of fluid (see figure 12*c*) indicating the explosive generation of turbulence. The results from all the simulated cycles are consistent with the ones described here, although there are some variations of the relative strength of the different flow elements.

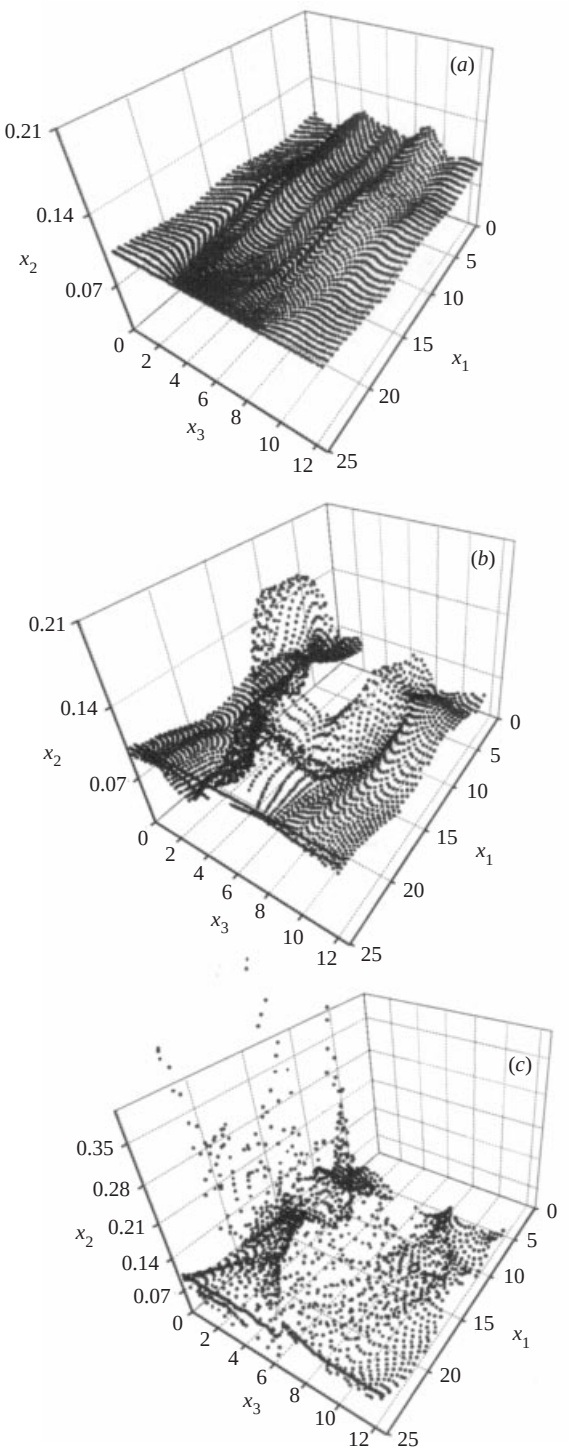

FIGURE 12. Visualization of markers continuously released along the line $x_1 = 25.13$, $x_2 = 0.1$ ($R_\delta = 800$ and wall A). (*a*) $t = 42.17\pi$; (*b*) $t = 42.47\pi$; (*c*) $t = 42.52\pi$.

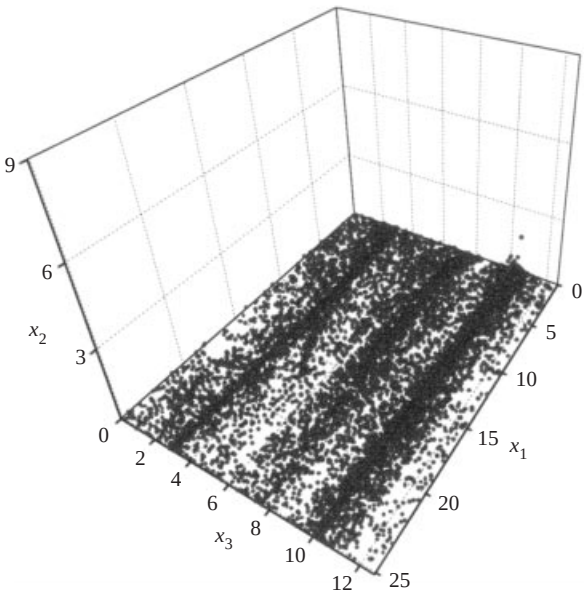

FIGURE 13. Visualization at $t = 42.17\pi$ of markers uniformly released at $x_2 = 0.1$ and $t = 41.5\pi$ ($R_\delta = 800$ and wall A).

3.2.2. *The vorticity field*

As previously pointed out, access to velocity, pressure, and vorticity fields in space and time allows a more detailed investigation of the flow close to the wall and a clear picture of the vortex structures which generate the marker streaks and their subsequent dynamics to be gained.

Figure 14 shows simultaneously the spanwise $\tilde{\Omega}_3$, vertical Ω_2 and streamwise Ω_1 vorticity components along with the streamwise velocity component at $x_2 = 0.163$ (x_2^* equal to about $3.9\nu^*/\overline{u_\tau^*}$) just before the end of the accelerating phase. Recall that $\tilde{\Omega}_3$ is the spanwise vorticity component after the subtraction of the vorticity averaged over the plane (x_1, x_3). Likewise, $\tilde{u}_1$ is the streamwise velocity component after the subtraction of the velocity averaged over the plane (x_1, x_3).

Figure 14 shows that the low-speed streaks are related to significant values of $\tilde{\Omega}_3$, which forms elongated vortex structures in the viscous sublayer (figure 14*b*). Indeed, strong spanwise vorticity is induced close to the wall by the large vertical gradient of the streamwise velocity. In the immediate vicinity of the wall $\tilde{u}_1 \sim -x_2\tilde{\Omega}_3$ and the contours of $\tilde{\Omega}_3$ mark the level of streamwise velocity at a fixed x_2.

In the literature (Sendstad & Moin 1992), low-speed streaks are also associated with significant values of the vertical component of vorticity which is generated by the spanwise gradients of the streamwise velocity. In fact, close to the wall, large contributions to Ω_2 come from $\partial\tilde{u}_1/\partial x_3$ and the Ω_2 structures indicate the side 'walls' of the low-velocity streaks. Figure 14(*c*) shows that, to observe significant values of Ω_2, it is necessary to move quite far from the wall, i.e. outside the viscous sublayer. Moreover, the analysis of the data shows that large values of the vertical component of vorticity appear between the regions of high- and low-speed fluid.

In the past low-speed streaks were thought to be originated by pairs of counter-rotating streamwise vortices located just outside the viscous sublayer. This idea has recently been questioned. In the steady flow case, as discussed by Moin & Mahesh (1998), the streamwise extent of the streamwise vortices outside the viscous sublayer

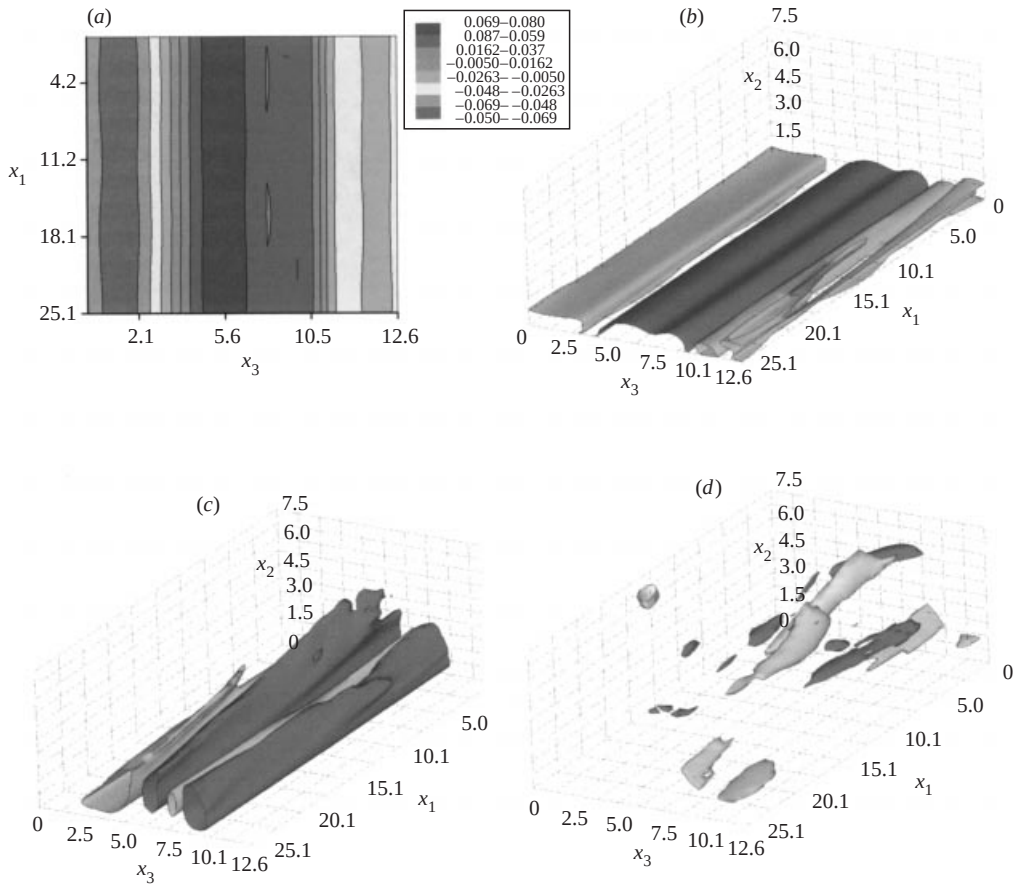

FIGURE 14. Velocity and vorticity fields at $t = 42.17\pi$ for $R_\delta = 800$ and wall A. (*a*) Streamwise velocity component $\tilde{u}_1$ at $x_2 = 0.163$. (*b*) Spanwise vorticity component $\tilde{\Omega}_3$. Isosurfaces for $|\tilde{\Omega}_3| = 0.12$. (*c*) Vertical vorticity component Ω_2. Isosurfaces for $|\Omega_2| = 0.12$. (*d*) Streamwise vorticity component Ω_1. Isosurfaces for $|\Omega_1| = 0.05$. (Light surfaces, positive values; dark surfaces, negative values.)

is much shorter than the low-speed streaks. In Moin & Mahesh (1998) the long streamwise length of the low-speed streaks appears to be due to a sequence of streamwise vortices following each other, pumping high-speed fluid toward the wall and low-speed fluid away from the wall (Sendstad & Moin 1992). An analysis of the vorticity field, which leads to the visualizations depicted in figure 12, shows neither the existence of long streamwise vortices nor the presence of a sequence of shorter alternating streamwise vortices (see figure 14*d*). Thus, it can be argued that low-speed streaks are not necessarily associated with the existence of streamwise vortices of any type. However, it should be noted that the results described so far have been obtained using the small computational box. Numerical experiments with smaller and larger boxes have shown that the small box captures the essential mechanism of turbulence generation and maintenance. However, as previously discussed, the results obtained (see also figure 2) show that the small box is not large enough to allow accurate predictions of all turbulence characteristics. Hence for $R_\delta = 800$ and wall A, a run has been made doubling the size of the computational box both in the streamwise and spanwise directions in such a way that $L^*_{x_1}$ and $L^*_{x_3}$ are approximately equal to 1290 and 640 average wall units respectively.

To understand the process which leads to the appearance of the low-speed streaks, attention has been focused on $\tilde{\Omega}_3$ which is plotted in figure 15 at different phases of the cycle during the early stages of formation of the low-speed streaks. Positive as well as negative patches of spanwise vorticity can be observed at $t = 41.53\pi$ near to the wall (see figure 15*a*). These vortices can be partly associated with the wall imperfections; a careful analysis of figure 15(*a*) shows that the vortex structures have their root at the crests and troughs of the wall waviness. As the flow decelerates, spanwise vortices of the same sign become aligned (see figure 15*b*) and tend to originate long vortex structures which are the starting point of the low-speed streaks (see figure 15*c*). To follow the time development of the low-speed streaks, in figure 16 $\tilde{\Omega}_3$ is plotted at subsequent phases of the cycle. In figure 16(*a*), the low-speed streaks formed by $\tilde{\Omega}_3$ are clearly detectable. The vortex structures appearing in figure 15(*c*) grow and spread along the wall till the low-speed streaks become more evident. Once formed low-speed streaks do not survive for a long time. Indeed, when the flow deceleration starts, the vortex structures generating the low-speed streaks begin to interact, sometimes becoming wavy. Then shortly after, they break into short segments and lose their coherence (see figure 16*b*, *c*). The breakup of the low-speed streaks starts at random locations (see figure 16*b*) and then it spreads along the whole plane (see figure 16*c*). Later on, small-scale vortices are present in the whole computational domain. Note that the break-up of the low-speed streaks does not take place always at the same phase of the cycle; sometimes it starts just at the beginning of flow deceleration, other times it takes place later, but always during the decelerating phase of the cycle. All these phenomena are in agreement with the dynamics of the tracers previously discussed referring to figures 12 and 14. Moreover, the vorticity fields shown in figures 15 and 16 are qualitatively similar to those shown in figure 14. Hence, it can be concluded that close to the wall the small and the large computational boxes provide similar results. On the other hand, differences between the results of the small box and those of the large box are found on moving outside the viscous wall layer and analysing the development of the streamwise vorticity component Ω_1. When the fluid starts to accelerate, only incoherent blobs of vorticity, generated by the burst events of the previous cycle, are present. Then, when the low-speed streaks tend to form, some streamwise vortices are formed close to the wall by the stretching and intensification of the incoherent vortex structures generated during the previous decelerating phase. This stretching takes place because of the large gradients in the vertical direction of the basic streamwise velocity component (Batchelor 1967). On the other hand, the vortices which are far from the wall tend to decay, being subject to a uniform translation. The streamwise vortices which form close to the wall organize themselves in the plane (x_1, x_3) (see figure 17) forming a sequence of vortices of alternating circulation aligned with the low-speed streaks and pumping low-speed fluid from the wall towards the fast moving fluid. Hence, the same basic process which is suggested to generate turbulence in steady flows can be recognized (Sendstad & Moin 1992).

Since the analysis of tracer trajectories and of isovorticity surfaces may be considered inadequate in detecting vortices in an unsteady flow, we have computed the eigenvalues of the symmetric tensor $\boldsymbol{D}^2 + \boldsymbol{\Omega}^2$ and we have considered the regions with two negative eigenvalues. As discussed by Jeong & Hussain (1995) these regions do indeed correlate well with coherent vortex structures buried in the background vorticity. Figure 18 visualizes an isosurface characterized by a negative value of λ_2, which is the second eigenvalue of the tensor $\boldsymbol{D}^2 + \boldsymbol{\Omega}^2$ ($\lambda_2 = -0.0015$). In figure 18 the same structures appearing in figure 17 can be recognized. Moreover, computing the cross-

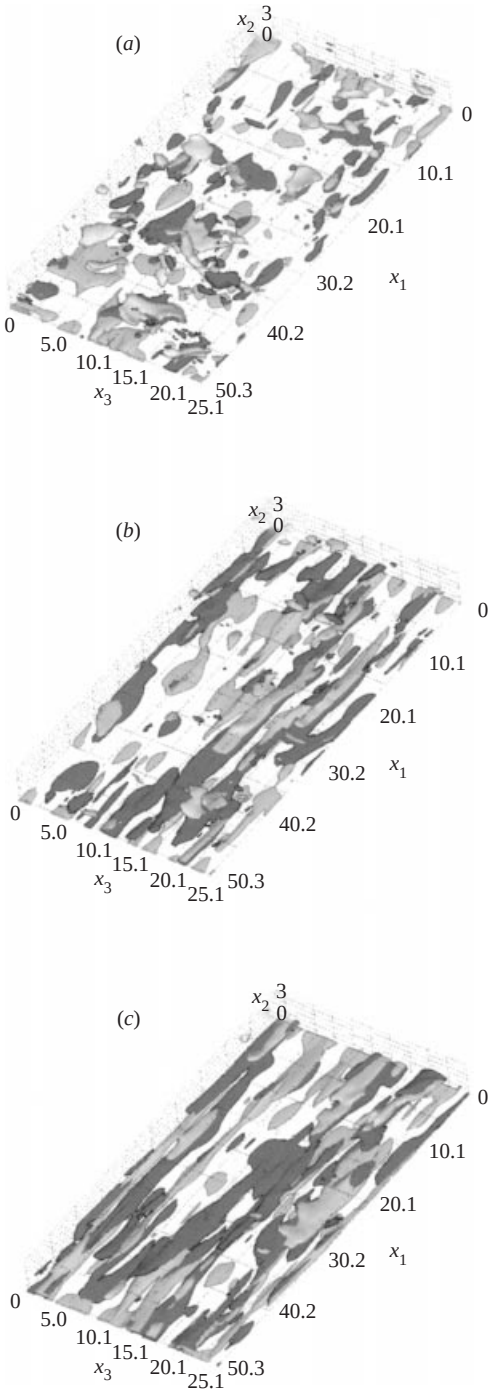

FIGURE 15. Spanwise vorticity component $\tilde{\Omega}_3$ for $R_\delta = 800$ and wall A. Isosurfaces for $|\tilde{\Omega}_3| = 0.15$ (light surface, positive values; dark surface, negative values). (*a*) $t = 42.53\pi$; (*b*) $t = 42.60\pi$; (*c*) $t = 42.66\pi$.

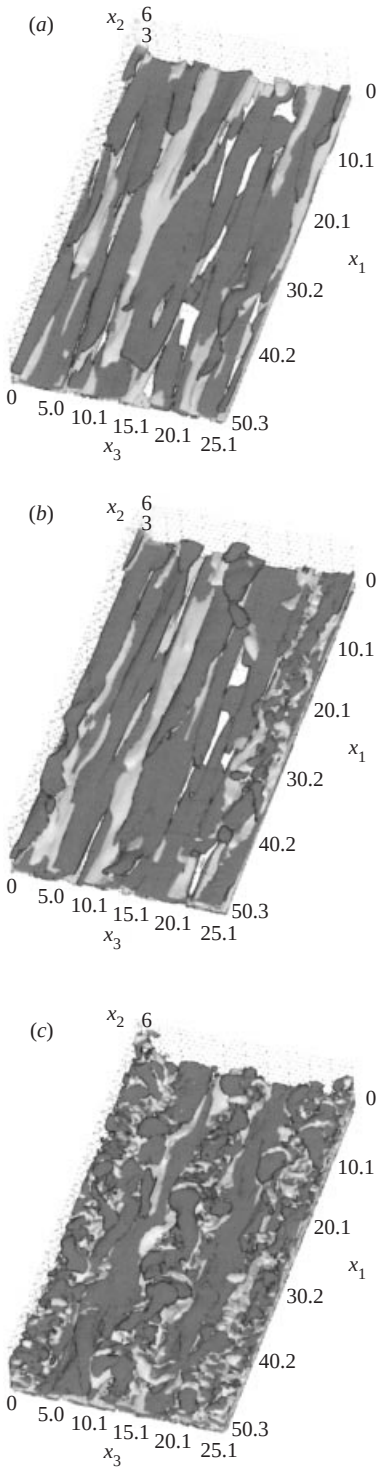

FIGURE 16. Spanwise vorticity component $\tilde{\Omega}_3$ for $R_\delta = 800$ and wall A. Isosurfaces for $|\tilde{\Omega}_3| = 0.15$ (light surface, positive values; dark surface, negative values). (*a*) $t = 42.82\pi$; (*b*) $t = 42.91\pi$; (*c*) $t = 43.00\pi$.

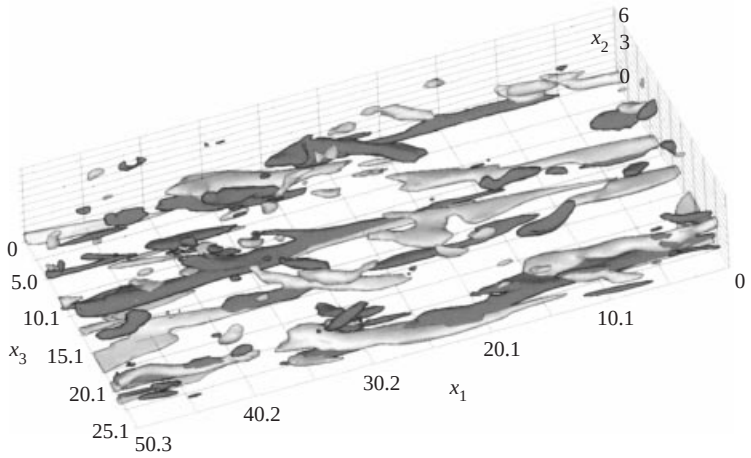

FIGURE 17. Streamwise vorticity component Ω_1 at $t = 42.82\pi$ for $R_\delta = 800$ and wall A. Isosurfaces for $|\Omega_1| = 0.08$ (light surface, positive values; dark surface, negative values).

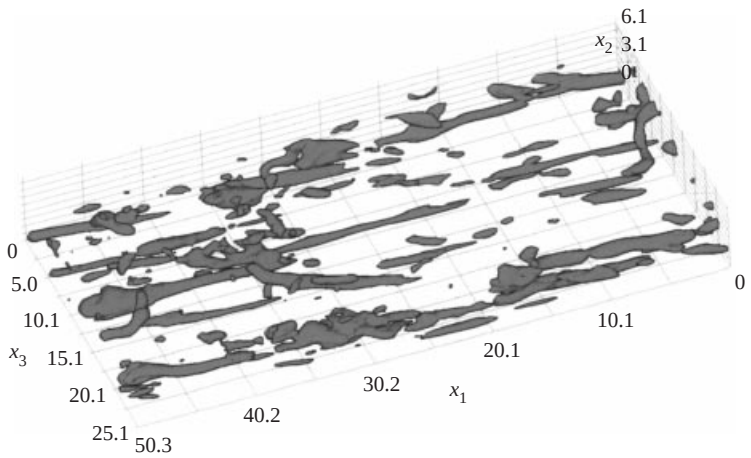

FIGURE 18. Isosurface of λ_2. $\lambda_2 = -0.0015$ at $t = 42.82\pi$ for $R_\delta = 800$ and wall A.

correlation coefficient of $-\lambda_2$ with each vorticity component, the cross-correlation between $-\lambda_2$ and $|\Omega_1|$ is found to be much higher than that between $-\lambda_2$ and $|\Omega_2|$ or $|\Omega_3|$. It can be concluded that the dominant near-wall educed coherent structures are highly elongated quasi-streamwise vortices. The vortices are of alternating sign, as shown in figure 17, and partially overlap in the x_1-direction in an almost ordered array. Moreover, the eduction approach by Jeong & Hussain (1995) also does not show the existence of hairpin vortices. Note also the lack of vortices having a streamwise length comparable to the length of the low-speed streaks. Finally, it is worth pointing out that the vorticity field associated with the low-speed streaks does not give rise to negative values of λ_2 within the viscous sublayer and hence coherent structures, as defined by Jeong & Hussain (1995), are absent here (Jeong *et al.* 1997).

3.2.3. *Turbulence structure*

To measure the spacing of the low-speed streaks many cycles have been simulated. Then the spanwise distribution of $\tilde{u}_1$ has been analysed. The quantity $\tilde{u}_1$ is defined as

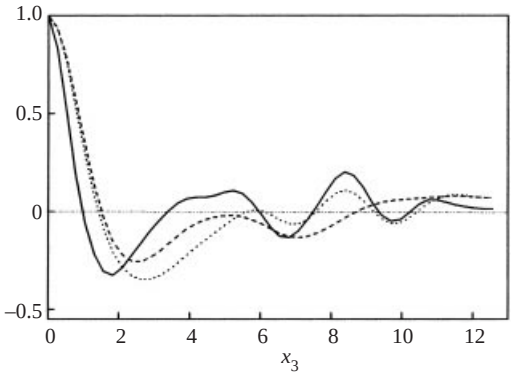

FIGURE 19. Two-point spatial autocorrelation function along the spanwise direction (large box) at $x_2 = 0.34$, $t = 42.87\pi$ and $R_\delta = 800$. Dashed line, spanwise velocity component; solid line, vertical velocity component; dotted line, streamwise velocity component.

$u_1 - \bar{u}_1$ where $\bar{u}_1$ is the value of u_1 averaged on the (x_1, x_3)-plane. It has been observed that the number of streaks depends on the phase of the cycle. The number of streaks is indeed larger at the end of the accelerating phases of the cycle when streaks start to appear. Then, some of them merge originating larger regions of low-speed fluid which remain stable for a relatively long period of time before breaking and originating small-scale vortices at the end of the decelerating phases, when bursts of turbulence appear.

The average spacing of the streaks has been determined by computing the two-point spatial auto-correlation of the streamwise velocity component $\tilde{u}_1$ in the spanwise direction. The analysis of the velocity field was made just before the break up of the low-speed streaks. This procedure has shown that a reproducible mean spacing exists, though there is a considerable variation in the spacing from cycle to cycle with a standard deviation of spacing of about 50%. A typical instantaneous autocorrelation function at $x_2 = 0.34$ for $R_\delta = 800$ is shown in figure 19; the values of the autocorrelation function averaged in the streamwise direction are plotted. Note that variations of $\tilde{u}_1$ in the streamwise direction are quite small (less than few per cent). The spacing of the low-speed streaks is evaluated by performing an average over 13 cycles. The results indicate that the average (spanwise) streak spacing corresponds approximatively to $5.3\delta^*$. Relating this value to the viscous length $\nu^*/\overline{u_\tau^*}$, one readily finds about $127\nu^*/\overline{u_\tau^*}$, which is a value close to the spacing observed in steady boundary layers. A somewhat smaller value is obtained if the instantaneous shear velocity is used.

When the coherent vortex structures associated with the low-speed streaks break up during the decelerating phases of the cycle, a large number of small vortices is generated. It is interesting to notice that the kinetic energy of turbulence starts to grow when the low-speed streaks appear. The strength of the coherent vortices associated with the low-speed streaks increases and so turbulence energy and Reynolds stresses grow too. Then the kinetic energy of turbulence attains its maximum when the coherent vortex structures begin to break up. The generation of small vortices implies large viscous effects and turbulence starts to damp. In figure 20 the vertically integrated specific kinetic energy $\mathscr{E}$ of turbulence,

$$\mathscr{E} = \frac{1}{L_{x_1} L_{x_3}} \int_0^{L_{x_1}} \int_0^{L_{x_2}} \int_0^{L_{x_3}} \tfrac{1}{2}((\tilde{u}_1)^2 + (u_2)^2 + (u_3)^2)\, \mathrm{d}x_1\, \mathrm{d}x_2\, \mathrm{d}x_3, \tag{10}$$

is plotted versus time. Looking at figure 16(a) where the spanwise vorticity component

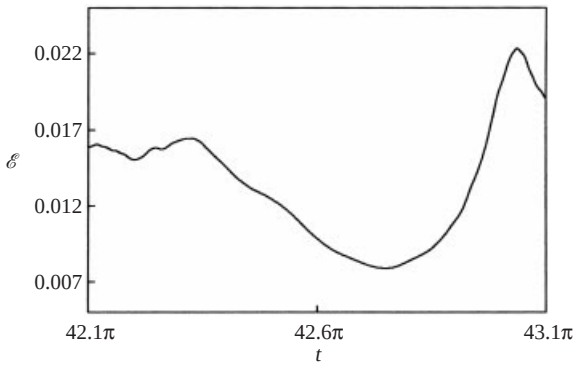

FIGURE 20. Specific kinetic energy $\mathscr{E}$ as defined in (10) ($R_\delta = 800$ and wall A).

is plotted at $t = 42.81\pi = 134.51$ just before the maximum of $\mathscr{E}$ is attained, and at figure 16(c), where the spanwise vorticity is plotted at $t = 43.01\pi = 135.11$ just after the maximum of $\mathscr{E}$, it can be verified that the damping of the turbulent kinetic energy is associated with the breaking of the coherent vortex structures originating the low-speed streaks.

To investigate the turbulence properties close to the wall, a statistical analysis of the velocity field has been made. As previously pointed out, the time history of plane-averaged quantities shows a stochastic and intermittent behaviour. The intermittency exposes the limited size of the computational box with respect to the largest vortex structures appearing in the boundary layer and the correspondingly small statistical sample. The cancellation of fluctuations for the small box involves phase-averaging the behaviour of a single quantity over a large number of cycles. The random spatial occurrence of large vortex structures in a natural turbulent wall layer is replaced here by a random occurrence during different cycles. However when the large vortex structures break into smaller vortices the size of the latter is much smaller than the computational box and a stochastic analysis of their characteristics can be attempted by defining the fluctuating component of any quantity as the actual value minus its plane-average value.

As experimentally observed by Hino *et al.* (1983), the probability density distribution of the fluctuating component $\tilde{u}_1$ of the streamwise velocity is skewed towards the positive side during most of the decelerating phase when turbulence appears (in discussing the distribution of $\tilde{u}_1$, positive values mean values of $\tilde{u}_1$ in the same direction as the average value of u_1 while positive values of u_2 mean vertical velocities in the upward direction). Moreover, the probability density distribution of the vertical velocity component u_2 turns out to be almost symmetric. Close to the wall and when turbulence first appears, further inspection of the probability density distributions classified according to the four categories of quadrants in the $(\tilde{u}_1, u_2)$-plane proposed by Brodkey, Wallace & Eckelmann (1974) discloses that the probability density distribution of $\tilde{u}_1$ is skewed towards the positive values of $\tilde{u}_1$ both when detecting values of $\tilde{u}_1 u_2 > 0$ and $\tilde{u}_1 u_2 < 0$. On the other hand, the probability density distribution of u_2 is skewed towards the positive when $\tilde{u}_1 u_2$ is positive (interactions), but it is reversed when $\tilde{u}_1 u_2$ is negative (ejection and sweep). Only when the two probabilities are superimposed does the probability density distribution of u_2 tend to become symmetric (see figure 21). However, a more careful analysis of the conditioned probability density function of u_2 shows that the skewness towards the positive values

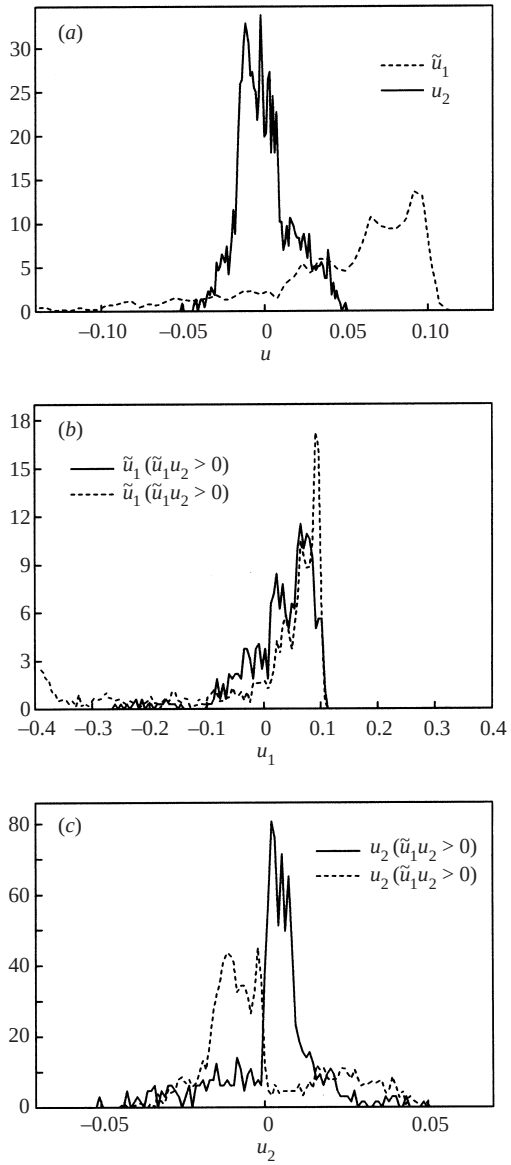

FIGURE 21. (*a*) Unconditioned probability density functions of $\tilde{u}_1$ and u_2. (*b*) Conditioned probability density functions of $\tilde{u}_1$. (*c*) Conditioned probability density functions of u_2'. ($R_\delta = 800$, wall A, $x_2 = 1.6$, $t = 42.47\pi$.)

which is present for $\tilde{u}_1 u_2 > 0$ is larger that the skewness towards the negative values when $\tilde{u}_1 u_2 < 0$. Since the unconditioned probability density function of u_2 turns out to be almost symmetric, it appears that not only are sweep events and outward interactions more frequent than ejection events and wall-ward interactions but also that sweep events tend to prevail on the outward interactions. This finding is confirmed by an analysis of the distribution of the events in the $(\tilde{u}_1, u_2)$-plane. Moreover, because of the continuity equation, which forces the plane-average value of u_2 to be zero, ejection events are less frequent but more violent that sweep events. A visualization of an ejection event is shown in figure 22 where the effect of the upward fluid motion

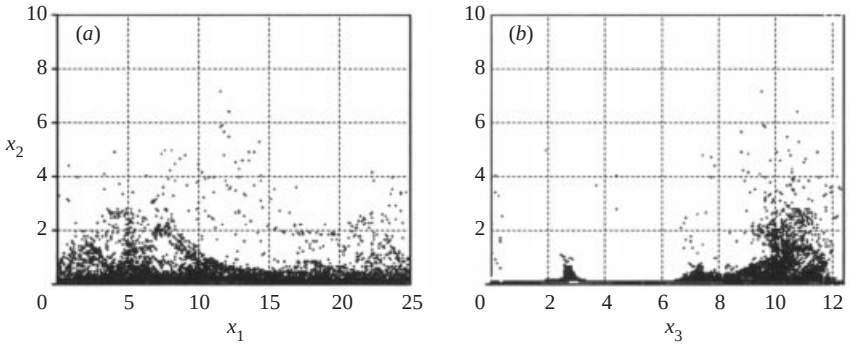

FIGURE 22. Visualization at $t = 42.23\pi$ of markers uniformly released at $x_2 = 0.1$ and $t = 41.50\pi$. (*a*) Side view, (*b*) front view ($R_\delta = 800$ and wall A).

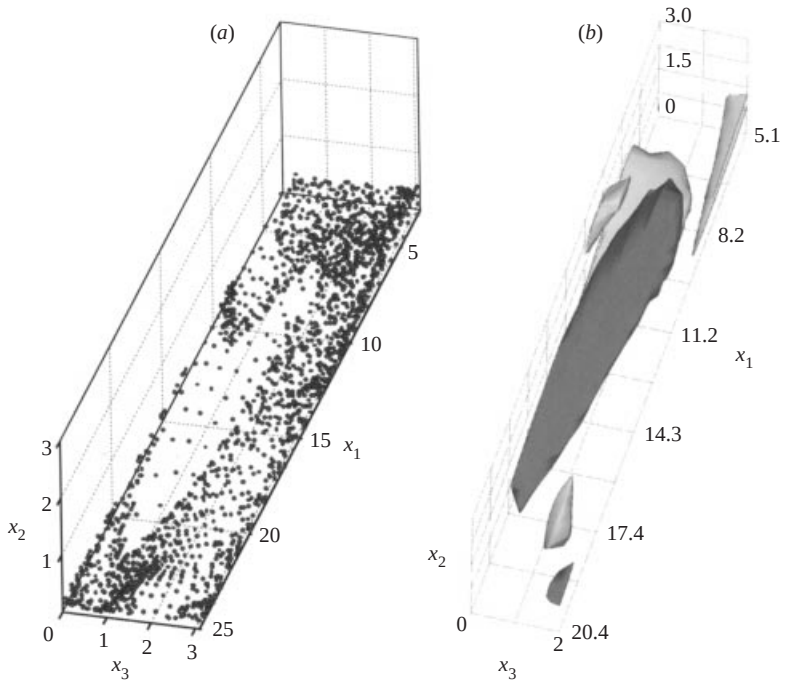

FIGURE 23. (*a*) Visualization at $t = 41.7\pi$ of markers uniformly released at $x_2 = 0.1$ and $t = 41.50\pi$. (*b*) Streamwise vorticity component Ω_1 at $t = 41.7\pi$. Isosurfaces for $|\Omega_1| = 0.04$ (light surface, positive values; dark surface, negative values). ($R_\delta = 800$ and wall A.)

on the passive tracers clearly appears. The markers are moved far from the wall (see figure 22*b*) and simultaneously in the downstream direction (see figure 22*a*) by an ejection event which takes place in a wall region identified by $0 < x_1 < 15$ and $9 < x_2 < 12$. A further ejection event appears around $x_2 = 3$. However, no evidence of coherent vortex structures associated with ejections, sweeps or interaction events has been found by analysing the vorticity field. Looking at the patterns formed by the passive tracers, uniformly released in a plane parallel to the wall during the final part of the decelerating phases and the early part of the accelerating phases, the tendency of the tracers to form arrow-shaped patterns is observed. These patterns, an example of which is shown in figure 23(*a*), are the result of the presence near the wall

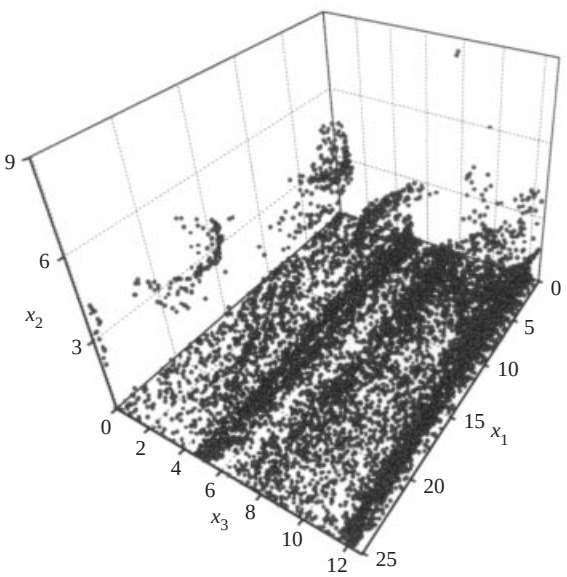

FIGURE 24. Visualization at $t = 41.13\pi$ of markers uniformly released at $x_2 = 0.1$ and $t = 40.50\pi$ ($R_\delta = 800$ and a flat wall).

of significant streamwise vortices similar to those shown in figure 17. As previously pointed out, these vortices form because of the stretching and intensification of the incoherent vortex structures generated by the breaking of the low-speed streaks (the stretching being due to the large velocity gradient present near to the wall) and induce large velocities which sweep the tracers away. Then secondary vorticity is generated at the wall and creates a new vortex structure which is driven away from the wall by the primary vortex. This process, in which a vortex near a no-slip wall induces secondary vorticity of opposite sign at the wall, carries it away to generate a new free vortex and then couples with it to form a rising pair, has been nicely observed in two-dimensional computations of vortex dipoles moving towards a wall (Orlandi 1990). Eventually, the process of low-speed streak formation repeats again during the following half-cycle.

3.3. *Influence of the amplitude of wall imperfections*

To show that in the intermittently turbulent regime the wall imperfections have no influence on the phenomenon, a simulation has been carried out for the same Reynolds number and a perfectly flat wall. The simulation started from a turbulent flow field obtained for an imperfect wall and then setting ϵ equal to zero. An example of the results obtained can be seen in figure 24 where the patterns formed by tracers uniformly released in a plane parallel to the wall are shown at the same phase as in figure 13. Some differences are present but the imperfect wall and the perfectly plane wall give the same streak spacing, if the phase average over many cycles is computed. Moreover, the gross features of the dynamics of the coherent vortex structures is always similar.

Hence it can be concluded that wall imperfections play a minor role in the intermittently turbulent regime where turbulence is self-sustaining. On the other hand, wall imperfections (or other external sources of perturbations) are found to play a fundamental role in the disturbed laminar regime. Indeed in the latter flow regime,

their presence is necessary to trigger the instability of the flow and to continuously feed the resonance mechanism. Moreover, the strength of the perturbations of the basic flow depends on the amplitude of the wall waviness and on its form. This finding explains why different experimentalists found different flow characteristics in this flow regime.

3.4. *Results at higher Reynolds numbers*

Up to now, results have been described for $R_\delta = 800$. When the Reynolds number is further increased, a larger number of vortices appear towards the end of the decelerating phases and turbulence activity spans over larger times and larger areas. However for the values of R_δ investigated here (up to 1200) these turbulent structures do not survive during the accelerating phases and the flow relaminarizes during the accelerating phases. Looking at the experimental results available in the literature it can be inferred that to simulate turbulence throughout the cycle, it would be necessary to consider values of the Reynolds number which cannot be simulated at present because of the large computational costs.

4. Conclusions

In this paper we describe the results of numerical simulations of the boundary layer generated close to a wall by a uniform oscillating pressure gradient (Stokes boundary layer). The flow is studied for values of the Reynolds number falling in the disturbed laminar and intermittently turbulent regimes. The wall is flat but with small imperfections which play a fundamental role in triggering transition to turbulence. The goal is to investigate the quasi-coherent vortex structures which form close to the wall and control momentum, mass and heat transfer. In the disturbed laminar regime the simulated vortex structures depend on the characteristics of wall imperfections and no general conclusion can be drawn. On the other hand, in the intermittently turbulent regime, the coherent vortex structures are found to be independent of the characteristics of wall imperfections. In the near-wall region, a sequence of events similar to those detected in steady boundary layers has been observed. In particular low-speed streaks, which start to appear towards the end of the accelerating phases, have been detected. Then, these low-speed streaks twist, oscillate and eventually break, generating small vortices which dissipate because of viscous effects. The analysis of the vorticity field has also shown the existence of a sequence of short streamwise vortices of alternating circulation pumping low-speed fluid far from the wall. Moreover, the present results suggest that the streak instability mechanism is the dominant mechanism generating and maintaining turbulence in oscillatory boundary layers. In fact no evidence of the well-known parent vortex structures spawning offspring vortices is found.

The authors are grateful to Professor Mutlu Sumer who made available the experimental data shown in figures 3, 4, 5. Many thanks are also due to Professor Roberto Verzicco for helpful discussions on various aspects of the numerical approach. The financial support of the University of Genova to one of the authors (P. C.) is gratefully acknowledged.

REFERENCES

Acarlar, M. S. & Smith, C. R. 1987 A study of hairpin vortices in a laminar boundary layer. Part 2. Hairpin vortices generated by fluid injection. *J. Fluid Mech.* **175**, 43–48.

Akhavan, R., Kamm, R. D. & Shapiro, A. H. 1991 An investigation of transition to turbulence in bounded oscillatory Stokes flows. Part 2. Numerical simulations. *J. Fluid Mech.* **225**, 423–444.

Batchelor, G. K. 1967 *An Introduction to Fluid Dynamics*. Cambridge University Press.

Beam, R. M. & Warming, R. F. 1976 An implicit finite-difference algorithm for hyperbolic system in conservative-low form. *J. Comput. Phys.* **22**, 87.

Blondeaux, P. 1990 Sand ripples under sea waves. Part 1. Ripple formation. *J. Fluid Mech.* **218**, 1–17.

Blondeaux, P. & Seminara, G. 1979 Transizione incipiente al fondo di un'onda di gravita'. *Rendi. Accad. Naz. Lincei* **67**, 407–417.

Blondeaux, P. & Vittori, G. 1994 Wall imperfections as a triggering mechanism for Stokes-layer transition. *J. Fluid Mech.* **264**, 107–135.

Blondeaux, P. & Vittori, G. 1999 Boundary layer and sediment dynamics under sea waves. *Adv. Coast. Ocean Engng* **4**, 133–190.

Brodkey, R. S., Wallace, J. M. & Eckelmann, H. 1974 Some properties of truncated turbulence signals in bounded shear flows. *J. Fluid Mech.* **63**, 209–224.

Corino, E. R. & Brodkey, R. S. 1969 A visual investigation of the wall region in turbulent flow. *J. Fluid Mech.* **37**, 1–39.

Corrsin, S. 1957 Some current problems in turbulent shear flows. In *Proc. 1st. Symp. on Naval Hydrodyn.* NAS-NRC Publ. 515, p. 373.

Falco, R. E. 1991 A coherent structure model of the turbulent boundary layer and its ability to predict Reynolds number dependence. *Phil. Trans. R. Soc. Lond.* A **336**, 103–129.

Ferrel, J. K., Richardson, F. M. & Beatty, K. O. 1955 Dye displacement technique for velocity distribution measurements. *Ind. Engng Chem.* **47**, 29–33.

Fishler, L. S. & Brodkey, R. S. 1991 Transition, turbulence and oscillating flow in a pipe. *Exps. Fluids* **11**, 388–398.

Hama, F. R. 1962 Streaklines in a perturbed shear flow. *Phys. Fluids* **5**, 644–650.

Hino, M., Kashiwayanagi, M., Nakayama, A. & Hara, T. 1983 Experiments on the turbulence statistics and the structure of a reciprocating oscillatory flow. *J. Fluid Mech.* **131**, 363–400.

Hussain, A. K. M. F. 1986 Coherent structures and turbulence. *J. Fluid Mech.* **173**, 303–356.

Jimenez, J. & Moin, P. 1991 The numerical flow unit in the near-wall turbulence. *J. Fluid Mech.* **225**, 213–240.

Jensen, B. L., Sumer, B. M. & Fredsoe, J. 1989 Turbulent oscillatory boundary layers at high Reynolds numbers. *J. Fluid Mech.* **206**, 265–297.

Jeong, J. & Hussain, F. 1995 On the identification of a vortex. *J. Fluid Mech.* **285**, 67–94.

Jeong, J., Hussain, F., Schoppa, W. & Kim, J. 1997 Coherent structures near the wall in a turbulent channel flow. *J. Fluid Mech.* **332**, 185–214.

Kim, J. & Moin, P. 1985 Application of a fractional-step method to incompressible Navier–Stokes equations. *J. Comput. Phys.* **59**, 308.

Kline, S. J. & Afgan, N. H. 1988 Near wall turbulence. *Proc 1988 Zorac Zaric Mem Conf.* Hemishere.

Moin, P. & Mahesh, K. 1998 Direct numerical simulation: a tool in turbulence research. *Annu. Rev. Fluid Mech.* **30**, 539–578.

Nychas, S. G., Hershey, H. C. & Brodkey, R. S. 1973 A visual study of turbulent shear flow. *J. Fluid Mech.* **61**, 513–540.

Orlandi, P. 1989 A numerical method for direct simulation of turbulence in complex geometries. *Annual Research Brief*, 215. Centre for Turbulence Research, Stanford University.

Rai, M. M. & Moin, P. 1991 Direct simulations of turbulent flow using finite-difference schemes. *J. Comput. Phys.* **96**, 15.

Robinson, S. K. 1991 Coherent motions in the turbulent boundary layer. *Annu. Rev. Fluid Mech.* **23**, 601–639.

Runstadler, P. W., Kline, S. J. & Reynolds, W. C. 1963 Experimental investigation of the flow structure of the turbulent boundary layer. *Dept. Mech. Engng, Stanford University, Rep.* MD-8.

Sarpkaya, T. 1993 Coherent structures in oscillatory boundary layers. *J. Fluid Mech.* **253**, 105–140.

Sendstad, O. & Moin, P. 1992 The near wall mechanics of three-dimensional turbulent boundary layer. *Rep.* TF-57, Thermosci. Div., Dept. Mech. Engng, Stanford University.

Spalart, P. R. & Baldwin, B. S. 1988 Direct simulation of a turbulent oscillating boundary layer. In *Turbulent Shear Flows* 6 (ed. J. C. André, J. Cousteix, F. Durst, B. Launder, F. Schmidt & J. Whitelaw). Springer.

Stokes, G. G. 1855 On the effects of internal friction of fluids on the motion of pendulums. *Trans. Camb. Phil. Soc.* **9**.

Verzicco, R. & Vittori, G. 1996 Direct simulation of transition in a Stokes boundary layer. *Phys. Fluids* **8**, 1341–1343.

Vittori, G. 1992 Flow field induced by sea waves over brick-pattern ripples. *J. Hydraulic. Engng ASCE* **118**, 1241.

Vittori, G. & Verzicco, R. 1998 Direct simulation of transition in an oscillatory boundary layer. *J. Fluid Mech.* **371**, 207–232.

Wu, X. 1992 The nonlinear evolution of high-frequency resonant triad waves in an oscillatory Stokes layer at high Reynolds number. *J. Fluid Mech.* **245**, 553–597.

Wu, X., Lee, S. S. & Cowley, S. J. 1993 on the weakly nonlinear three-dimensional instability of shear layers to pairs of oblique waves: the Stokes layer as a paradigm. *J. Fluid Mech.* **253**, 681–721.